Zonostrophic turbulence in the subsurface oceans of the Jovian and Saturnian moons

Simon Cabanes, Thomas Gastine, Alexandre Fournier

Icarus 415 (2024) 116047

Contents lists available at ScienceDirect

Icarus

journal homepage: www.elsevier.com/locate/icarus

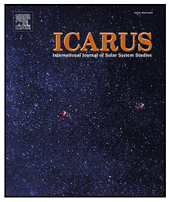

Research Paper

Zonostrophic turbulence in the subsurface oceans of the Jovian and Saturnian moons

Simon Cabanes *, Thomas Gastine, Alexandre Fournier

Université Paris Cité, Institut de physique du globe de Paris, UMR 7154 CNRS, 1 rue Jussieu, F-75005, Paris, France

ARTICLE INFO

Keywords:
Icy moons
Ocean dynamics
Zonostrophy
Rotating convection

ABSTRACT

In order to characterize the global circulation of the subsurface ocean of Jovian and Saturnian moons, we analyse the properties of 21 three-dimensional simulations of Boussinesq thermal convection in a rapidly rotating spherical shell. Flow is driven by an adverse temperature contrast imposed across the domain, and is subjected to no-slip boundary conditions. We cover a region of parameter space previously unexplored by global simulations, both in terms of rapid rotation and vigour of convective forcing, closer to, yet still admittedly far from, the conditions appropriate for the subsurface ocean of Ganymede, Europa, Enceladus, and Titan. Our most extreme simulations exhibit a dynamic global circulation that combines powerful east–west zonal jets, planetary waves, and vortices. A spectral analysis of the kinetic energy distribution performed in cylindrical geometry reveals a high degree of anisotropy of the simulated flows. Specifically, the axisymmetric zonal energy spectra follow a steep -5 slope in wavenumber space, with the energy amplitude exclusively controlled by the rotation rate. In contrast, the non-axisymmetric residual spectra display a gentle $-5/3$ slope, with the energy amplitude controlled by the thermal buoyancy input power. This spectral behaviour conforms with the theory of zonostrophic turbulence, as coined by Sukoriansky et al. (2002), and allows us to propose tentative extrapolations of these findings to the more extreme conditions of icy satellites. By assuming that kinetic energy dissipates via Ekman friction at the ice–ocean boundary, we predict an upper bound for the geostrophic zonal velocity ranging from a few centimetres per second for Enceladus to about one metre per second for Ganymede, with residual velocities smaller than the zonal velocity by an order of magnitude on each moon. These predictions yield typical jets size approaching the ocean depth of Titan, Ganymede and Europa and 10 to 40% of the ocean depth on Enceladus.

1. Introduction

The astrobiological potential of the Jovian and Saturnian moons, most notably Europa, Ganymede, Enceladus, and Titan, has come to the fore in the wake of the Galileo, Cassini–Huygens, and Juno space missions. These satellites contain more than water: non-aqueous components, including salts and sulphur, have been detected on the surface of Enceladus, while organic materials have been identified within plumes emanating from geysers at its South pole (Postberg et al., 2011, 2018). While Hsu et al. (2015) have provided persuasive indications of silica nanoparticles on the same Enceladus, spectroscopic analyses have revealed the presence of diverse salts, such as $MgSO_4$, NaCl, NH_4Cl, as well as sulphur compounds and organic materials on the surfaces of Europa (Carlson et al., 2009) and Ganymede (Tosi et al., 2023). This catalog of observations points to a well-mixed subsurface ocean and a substantial hydrothermal activity inside these moons.

The concealed ocean of these icy satellites plays a crucial role in shaping their surface composition (see the review by Soderlund et al., 2020). A good description of its circulation is key, since it governs the transport of heat and matter from the floor up to the icy crust and back. To date, most of our knowledge on the dynamics of subsurface oceans relies on the outcome of global first-principle simulations. These simulations drive oceanic flow either by thermal convection (e.g. Soderlund et al., 2014), mechanical forcing (e.g., tides or libration Grannan et al., 2017; Lemasquerier et al., 2017), or even magnetic forcing due to electromagnetic pumping in the case of Europa (Gissinger and Petitdemange, 2019). Recent numerical investigations have also explored the effects of heat flux variations from the inner mantle (Terra-Nova et al., 2023) and temperature fluctuations beneath the ice shell on oceanic convection dynamics (Kang et al., 2022). In these studies, the resulting flows promote turbulent mixing within the bulk ocean and thermo-compositional gradients, which have significant implications for the ice shell, transport properties, surface geology, and potential habitability. Nevertheless, bridging the gap between this research and

* Corresponding author.
E-mail address: cabanes@ipgp.fr (S. Cabanes).

https://doi.org/10.1016/j.icarus.2024.116047
Received 14 November 2023; Received in revised form 4 March 2024; Accepted 11 March 2024
Available online 13 March 2024

in situ observations remains an intricate challenge, demanding further exploration and validation.

Addressing this challenge, several studies have proposed the possibility of connecting thermal convection in the subsurface ocean to the variations of the ice shell thickness inferred from space missions (Kvorka et al., 2018). Numerical simulations of rotating convection in spherical shells conducted by Amit et al. (2020), Soderlund et al. (2014), Soderlund (2019), Kvorka and Čadek (2022) and Gastine and Aurnou (2023) demonstrate that planetary rotation results in a pronounced latitudinal dependence of the flow, which impacts the heat flux across the outer surface. Regions with high heat flux are more likely to experience increased melting, providing a potential link between observed ice shell topography and the behaviour of the underlying ocean. However, no consensus has emerged among these studies regarding the flow patterns characterizing each satellite. This lack of consensus may stem from variations in the boundary conditions prescribed by the authors, as well as from the discrepancies between the planetary regimes and those achieved numerically.

The forthcoming NASA's Europa Clipper mission (Roberts et al., 2023) and ESA's JUICE mission (Grasset et al., 2013) will provide additional data on surfacial heat flux and ice topography, which should reinvigorate ongoing debates and shed new light on ocean dynamics.

In the meantime, we propose in this study to resort to a predictive theoretical approach to unveil the dynamics of the subsurface oceans, capitalizing on progress made over the past two decades in the topic of rotating turbulence. Our working assumption is that oceanic flow is driven by thermal convection alone. We will calibrate our theory using a suite of numerical simulations, for subsequent extrapolation to the oceans of the Jovian and Saturnian moons.

The simulations involve a spherical fluid layer of thickness D confined between two rigid boundaries, which rotates at a constant rotation rate Ω. Convective motions are driven by a fixed temperature contrast ΔT imposed between the two boundaries. The ratio of the inner radius of the shell to its outer radius is set to 0.8. The fluid mechanical problem at hand is controlled by three dimensionless numbers: the Ekman number $E = \nu/\Omega D^2$, the Rayleigh number $Ra = \alpha g_o D^3 \Delta T/\nu\kappa$, and the Prandtl number $Pr = \nu/\kappa$, where ν and κ are the viscous and thermal diffusivities, α is the thermal expansivity, and g_o is the acceleration of gravity at the surface of the domain.

In this context, it is common practice to refer to the regime diagram for rotating convection initially introduced by Gastine et al. (2016). Fig. 1 replicates and extends this diagram by incorporating additional studies that deal with the subsurface oceans of the icy moons. The onset of convection is determined by the critical Rayleigh number Ra_C and is expected to follow $Ra_C \sim E^{-4/3}$ in the limit of vanishing Ekman numbers. The exact values shown by black crosses in Fig. 1 come from the linear computations by Barik et al. (2023) for a spherical shell with our adopted radius ratio of 0.8. The parameter space $(E, RaE^{4/3})$ is divided into several dynamical regimes. Beyond the weakly non-linear regime close to onset, and for Rayleigh numbers below Ra_R, the influence of rotation is maximum, resulting in a predominantly geostrophic flow where the balance between Coriolis force and pressure gradient leads to a strong flow invariance along the direction of rotation. For Rayleigh numbers exceeding Ra_{NR}, the influence of rotation is lost and the flow is dominated by fluid inertia. In between, a transitional regime prevails, with a weak but still significant influence of rotation. Given the ongoing debates regarding the scaling laws for Ra_{NR}, we report in Fig. 1 two possible transition parameters (see Gastine et al., 2016; Cheng et al., 2018, for more details). Note also that these regime boundaries are susceptible to change with the radius ratio of the fluid domain.

In addition to the new calculations performed for this study, Fig. 1 also includes simulations of 3D convection by Soderlund et al. (2014), Amit et al. (2020), Kvorka and Čadek (2022) and Bire et al. (2022). The numerical cost of such global simulations makes it necessary to operate with enhanced values of the fluid kinematic viscosity ν and thermal diffusivity κ. Employing physically sound no-slip (also termed rigid) boundary conditions, as done e.g. by Amit et al. (2020), may tend to exaggerate the role played by viscous stresses in the dynamics. This led several authors (e.g. Soderlund et al., 2014; Soderlund, 2019; Kvorka and Čadek, 2022) to opt for the more questionable free-slip boundary conditions. Additionally, simulations from Bire et al. (2022), computed in a spherical wedge geometry, considered a hybrid combination of no-slip at the bottom boundary and free-slip at the top boundary.

The generic picture that emerges from these previous studies is that convective motions are significantly influenced by the relative importance of rotation. Rotation enforces flow invariance along the rotation axis and fosters the formation of large-scale, axisymmetric (invariant in azimuth) flows known as zonal jets (e.g. Christensen, 2002). Bire et al. (2022) show that the zonal flow pattern takes the form of multiple jets of alternated directions with a weak prograde jet at the equator (see their Fig. 6). At larger convective forcings (when $Ra \sim E^{-2}Pr$), the zonal flow pattern transitions to a three-jet configuration dominated by a strong retrograde equatorial jet (see, e.g. Soderlund, 2019, her Fig. 2). In these prior studies, free-slip boundary conditions have been shown to promote stronger jets than those obtained in a no-slip configuration. When free-slip boundaries are employed, zonal flows dominate the kinetic energy budget, for instance reaching up to 98% of the total energy at $E = 10^{-5}$ in the simulations by Yadav et al. (2016), while this fraction is much smaller in simulations that adopt no-slip boundaries, for instance $\sim 50\%$ at $E = 3 \times 10^{-7}$ in Gastine and Aurnou (2023).

Following Soderlund (2019), one can estimate the Ekman and Rayleigh numbers of the icy satellites and locate them in the regime diagram (see the coloured polygons in Fig. 1). Since these estimates fall within the transitional regime, the flow of the subsurface oceans is expected to be influenced by planetary rotation. Also, the circulation of Enceladus is likely to be more rotationally-constrained than that of Ganymede, Europa, and Titan, which are closer to the boundary of the non-rotating regime.

In any event, the force balance of interest in this study is such that the Coriolis force dominates both viscous stresses and, to a lesser extent, inertia. In terms of dimensionless numbers, this implies that $E \ll 1$ and that the Rossby number $Ro = U/\Omega D$ (here U is a typical flow velocity) is below unity. Such flows, because they are essentially two-dimensional (2D), transfer energy upscale through non-linear processes known as turbulent cascades (Kraichnan, 1967). In addition, the spherical geometry of planetary fluid layers enforce a zonal anisotropization of the turbulent cascades to form east–west jets via the so-called β-effect (Rhines, 1975). These specific planetary conditions define the regime of zonostrophic turbulence (Sukoriansky et al., 2002).

In the framework of 2D-turbulence, Sukoriansky et al. (2002) provided scaling laws that govern the statistical distribution of kinetic energy in zonostrophic flows. Fig. 2 illustrates this theoretical distribution against wavenumber k, where each wavenumber corresponds to a specific scale of motion. Zonostrophic turbulent flows exhibit universal kinetic energy spectra. The zonal (axisymmetric) component follows a steep k^{-5} slope, while the residual (non-axisymmetric) component adheres to the classical Kolmogorov–Batchelor–Kraichnan (KBK) scaling with a $k^{-5/3}$ slope. Also, the magnitude of the zonal spectrum solely depends on the rotation rate and some geometric parameters of the fluid shell, while the magnitude of the residual spectrum is determined by the turbulent power injected at wavenumber k_i (see below for details). According to Sukoriansky et al. (2002), a flow is considered zonostrophic when an inertial range exists between the friction-dominated wavenumber k_f and the residual-dominated wavenumber k_β, as illustrated in Fig. 2. In that range, zonal energy surpasses its residual counterpart. Large-scale Ekman friction, which is contingent upon the prescription of no-slip boundary conditions, impedes energy transfer to smaller wavenumbers ($k < k_f$). This upscale transfer is possible for free-slip simulations, which may lead to overestimate the global kinetic energy budget.

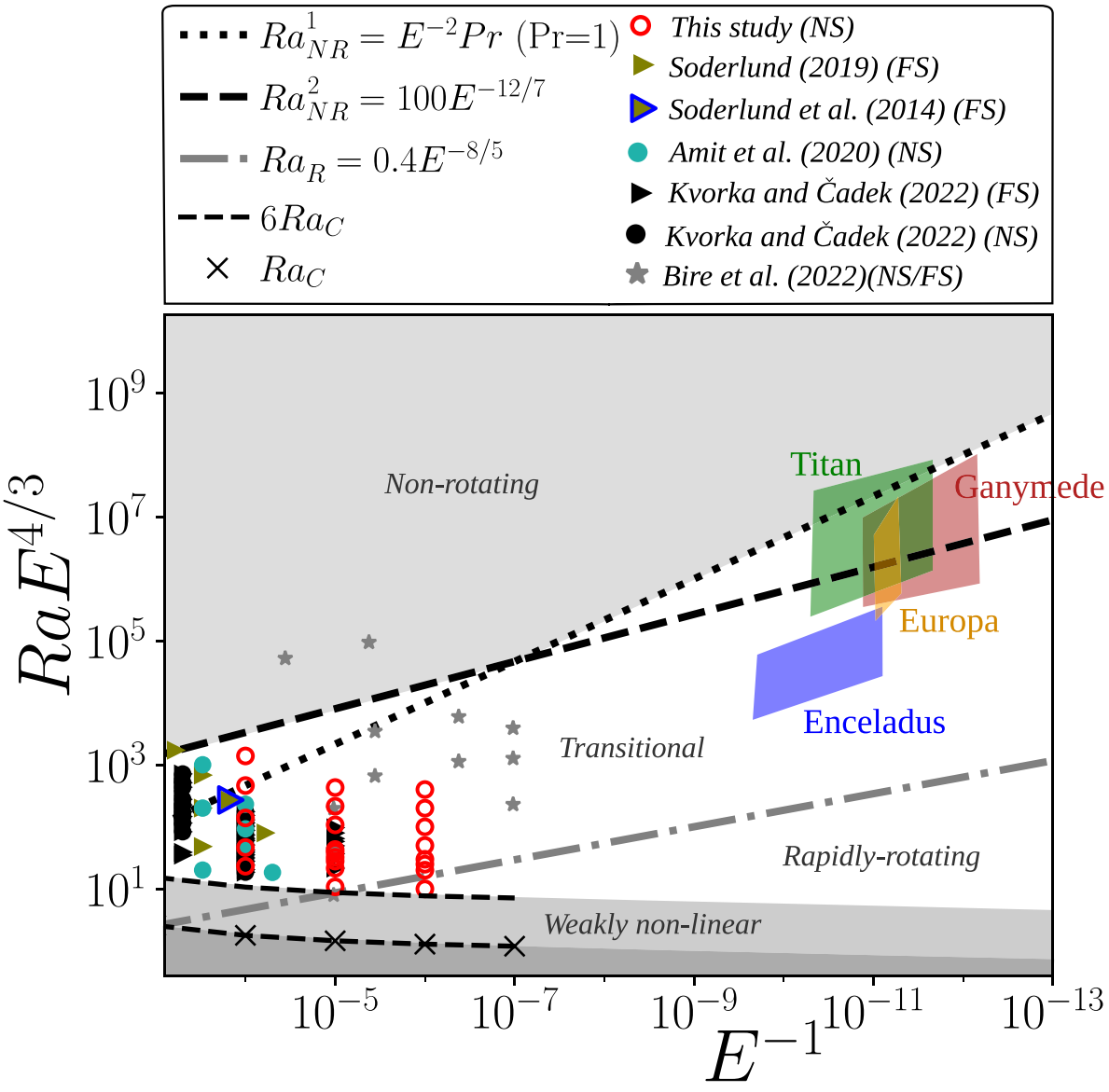

Fig. 1. Convective regime diagram following (Gastine et al., 2016) with superimposed parameter estimates for Enceladus (blue), Titan (green), Europa (yellow), and Ganymede (red) as outlined in Appendix B and Table B.3 and following the calculation provided in Soderlund (2019). Direct numerical simulations from the current study and from Soderlund (2019), Amit et al. (2020), Kvorka and Čadek (2022) and Bire et al. (2022) are reported with circles/triangles for no-slip(NS)/free-slip(FS) boundary conditions. The black crosses denote the critical Rayleigh number Ra_C given by Barik et al. (2023) for each Ekman number and a radius ratio of 0.8. The boundary $6\,Ra_C$ delimits the weakly non-linear regime defined by Gastine et al. (2016) for a radius ratio of 0.6. Straight lines are predicted transitions from the regime of geostrophic turbulence to a transitional regime less influenced by rotation (grey line), and from the transitional regime to a non-rotating regime (black lines). Scaling laws for Ra_R and Ra^1_{NR} are taken from Gastine et al. (2016) and for Ra^2_{NR} from Gilman (1977). (For interpretation of the references to colour in this figure legend, the reader is referred to the web version of this article.)

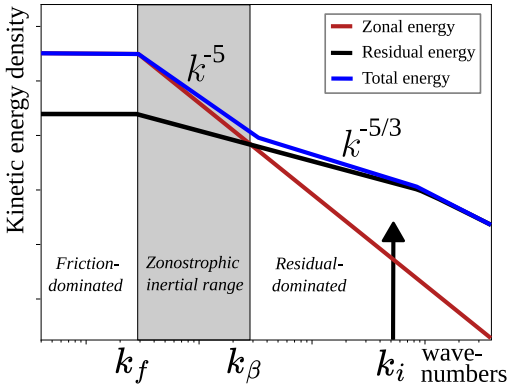

Fig. 2. Theoretical kinetic energy distribution as a function of wavenumber k in zonostrophic turbulence, after Galperin et al. (2010) and Cabanes et al. (2020).

To date, spectral distributions such as the one sketched in Fig. 2 have been detected in Jupiter's tropospheric winds (Galperin et al., 2014; Young and Read, 2017), in mechanically forced laboratory experiments (Read et al., 2015; Cabanes et al., 2017; Galperin et al., 2016; Lemasquerier et al., 2023), in numerical simulations on a rotating sphere (Huang et al., 2001; Galperin et al., 2006) as well as in global circulation atmospheric models (Cabanes et al., 2020). However, this particular regime has not yet been observed in analog experiments replicating rotating convection.

Indeed, despite the substantial body of research demonstrating that rotating convection exhibits the essential ingredients of zonostrophic turbulence, it remains a loosely-documented aspect. For instance, upscale turbulent cascades have been studied in three-dimensional (3D) simulations of rapidly rotating Rayleigh–Bénard convection (Favier et al., 2014; Kunnen et al., 2016; Maffei et al., 2021). Carrying out a flow analysis, Böning et al. (2023) provided compelling evidence that

planetary jets can be driven through statistical correlations of small turbulent scales in 3D spherical convection. Additionally, the formation of zonal jets has been observed in simulations replicating conditions akin to those found within the Earth's liquid core (Guervilly and Cardin, 2017) and the deep convective envelope of Jupiter and Saturn (Aurnou and Olson, 2001; Heimpel et al., 2005; Yadav and Bloxham, 2020). In light of these findings, our first goal is to demonstrate the adequacy of zonostrophic theory to account for the statistical properties of rotating convective flows located in the transitional region of Fig. 1, keeping in mind for later that the applicability of this theory might become questionable when approaching the regime of non-rotating convection.

Subsequently, we intend to make use of this theoretical framework to assess the kinetic energy budget and flow regimes within the oceans of Europa, Ganymede, Enceladus, and Titan. Previous attempts to predict subsurface ocean flows have relied on scaling arguments, drawing an hypothetical equivalence between the Rossby number of the numerical simulations and that of the actual oceanic flows (e.g. Vance et al., 2021; Bire et al., 2022). In addition, since the simulations in question adopt free-slip boundary conditions, they neglect friction effects, which may lead to overestimate the global energy budget. Alternatively, Jansen et al. (2023) utilize energetic constraints to infer flow velocity within the subsurface oceans, under the assumption that dissipation is controlled by a turbulent quadratic drag akin to that of the Earth's ocean (Jansen, 2016). Employing a comparable approach, but with a different assumption regarding the nature of dissipative processes, we provide an upper bound for the zonal flow velocity. Drawing upon the theory of zonostrophic turbulence, we derive the typical scale of zonal jets in subsurface oceans, along with the residual velocity.

To this end, we conduct 21 high-resolution simulations of 3D convective turbulence in a spherical shell. We explore a parameter range that reaches Ekman numbers smaller by at least one order of magnitude with respect to previous studies (recall Fig. 1). We present in Section 2 the governing equations, numerical method, parameter coverage, and key diagnostics used in this study. In Section 3, we present global properties of the kinetic energy in our numerical simulations and we conduct a statistical analysis of the zonal (axisymmetric) and residual (non-axisymmetric) flow components using cylindrical harmonic functions. In Section 4 we delve into the insights offered by the theory of zonostrophic turbulence to explore the icy satellites' oceans. Thanks to estimates of the oceans' depth, the rotation rate of the moons and the heat flux coming up from their interiors we produce predictive kinetic energy budgets for Enceladus, Titan, Europa and Ganymede's oceans. Finally, in Section 5, we introduce a novel and complementary regime diagram that combines Ekman and Rossby numbers.

2. Hydrodynamical model

2.1. Governing equations

We consider rotating convection of a Boussinesq fluid confined in a spherical shell. The fluid shell rotates at a constant angular frequency Ω about the axis z. Convective motions are driven by a fixed temperature contrast $\Delta T = T_i - T_o$ between the inner radius r_i and the outer radius r_o of the sphere. Boundaries are impermeable, no-slip and held at constant temperatures. We adopt a dimensionless formulation of the Navier–Stokes equations using the shell thickness $D = r_o - r_i$ as the reference length scale and the inverse rotation rate Ω^{-1} as the reference time scale. The temperature contrast ΔT defines the temperature scale and gravity is non-dimensionalized using its reference value at the outer boundary g_o. The dimensionless equations that govern convective motions for the velocity $\mathbf{u}$, the pressure p and the temperature T are expressed by

$$\begin{aligned} \nabla\cdot\mathbf{u} &= 0, \\ \frac{\partial\mathbf{u}}{\partial t} + \mathbf{u}\cdot\boldsymbol{\nabla}\mathbf{u} + 2\mathbf{e}_z\times\mathbf{u} &= -\nabla p + \frac{Ra\,E^2}{Pr} gT\mathbf{e}_r + E\boldsymbol{\nabla}^2\mathbf{u}, \\ \frac{\partial T}{\partial t} + \mathbf{u}\cdot\boldsymbol{\nabla}T &= \frac{E}{Pr}\nabla^2 T\,. \end{aligned} \tag{1}$$

The unit vectors in the radial and vertical directions are denoted by $\mathbf{e}_r$ and $\mathbf{e}_z$, respectively. The system of Eqs. (1) is governed by three dimensionless numbers, the Ekman number E, the Rayleigh number Ra and the Prandtl number Pr defined above. The radius ratio of the spherical shell is $\eta = r_i/r_o$. To compare with previous studies, we adopt a linearly varying gravity with $g = r/r_o$.

2.2. Numerical method and parameter coverage

Numerical simulations have been computed using the open source pseudospectral code `MagIC`[1] (the reader is referred to Wicht, 2002; Gastine et al., 2016, for more details) and the open-source library `SHTns` for the spherical harmonic transforms (Schaeffer, 2013).[2] The system of Eqs. (1) is solved in spherical coordinates (r,θ,ϕ) and the velocity and temperature fields are expanded in spherical harmonic functions up to degree $\ell_{\max}$ in colatitude θ and longitude ϕ and in Chebyshev polynomials up to degree N_r along the radius. The time integration is performed using the ARS343 semi-implicit time scheme (Ascher et al., 1997; Gopinath et al., 2022). We build a dataset of 21 numerical simulations, with a fixed Prandtl number of one and covering the parameter range $10^{-6} \le E \le 10^{-4}$ and $10^7 \le Ra \le 2\times10^{10}$. The full set of simulations and related numerical truncation are given in Table 1. To mitigate the numerical cost and allow an exploration of lower Ekman numbers, the radius ratio is set to $\eta = 0.8$, which lies in the low range expected for the subsurface oceans in the Solar System (see Table B.3).

2.3. Diagnostics

In order to assess the influence of the various control parameters on the global flow properties, we define several diagnostic quantities. We adopt the following notations regarding different averaging procedures. Overbars $\overline{\cdots}$ correspond to a time average, $\langle\cdots\rangle$ to a spatial average over the whole volume and $\langle\cdots\rangle_\phi$ to an azimuthal average

$$\overline{f} = \frac{1}{\tau}\int_{t_o}^{t_o+\tau} f\,\mathrm{d}t,\ \langle f\rangle = \frac{1}{V}\int_V f\,\mathrm{d}V,\ \langle f\rangle_\phi = \frac{1}{2\pi}\int_0^{2\pi} f\,\mathrm{d}\phi, \tag{2}$$

where τ is the time averaging interval and V is the volume of the spherical shell.

The dimensionless total kinetic energy E_T is defined by

$$E_T = \frac{1}{2}\overline{\langle u^2\rangle} = \sum_{\ell=1}^{\ell_{\max}}\sum_{m=0}^{\ell}\overline{\varepsilon_\ell^m}, \tag{3}$$

where ε_ℓ^m is the dimensionless kinetic energy density at spherical harmonic degree ℓ and order m. A typical dimensionless flow velocity is given by the time-averaged Rossby number, defined as

$$Ro = \sqrt{2E_T}. \tag{4}$$

In the context of spherical rotating turbulence, it is relevant to distinguish the axisymmetric flow (or zonal flow hereafter) from its residual, non-axisymmetric counterpart. We hence define the dimensionless zonal kinetic energy and its associated Rossby number

$$E_Z = \frac{1}{2V}\int_V \overline{\langle u_\phi\rangle_\phi^2}\mathrm{d}V = \sum_{\ell=1}^{\ell_{\max}}\overline{\varepsilon_\ell^0} \quad\text{and}\quad Ro_Z = \sqrt{2E_Z}, \tag{5}$$

where the contribution of the non-axisymmetric modes ($m \neq 0$) are excluded. The dimensionless residual kinetic energy and its associated Rossby number are defined by

$$E_R = \sum_{\ell=1}^{\ell_{\max}}\sum_{m=1}^{\ell}\overline{\varepsilon_\ell^m} \quad\text{and}\quad Ro_R = \sqrt{2E_R}, \tag{6}$$

[1] available at https://github.com/magic-sph/magic

[2] available at https://gricad-gitlab.univ-grenoble-alpes.fr/schaeffn/shtns

Table 1
Summary of the 21 simulations performed in this study. E and Ra are the input Ekman and Rayleigh numbers, respectively. $N_r \times \ell_{max}$ defines the numerical truncation. The five rightmost columns feature diagnostic parameters such as the Rossby number Ro, the energy ratios E_Z/E_T, E_Z^g/E_Z, E_R^g/E_R, and the zonostrophy index R_β (see text for details).

N°	E	Ra	$N_r \times \ell_{max}$	Ro	E_Z/E_T	E_Z^g/E_Z	E_R^g/E_R	R_β
1	10^{-6}	1×10^9	257×682	6.3×10^{-4}	0.17	0.99	0.85	1.18
2	10^{-6}	2×10^9	321×1024	1.6×10^{-3}	0.38	0.99	0.77	1.37
3	10^{-6}	2.5×10^9	321×1024	2.0×10^{-3}	0.43	0.99	0.77	1.39
4	10^{-6}	3×10^9	385×1365	2.4×10^{-3}	0.42	0.99	0.70	1.42
5	10^{-6}	5×10^9	385×1365	4.0×10^{-3}	0.46	1.00	0.64	1.44
6	10^{-6}	1×10^{10}	513×1365	6.7×10^{-3}	0.36	0.99	0.59	1.40
7	10^{-6}	2×10^{10}	705×1365	1.1×10^{-2}	0.30	0.99	0.47	1.34
8	10^{-5}	5×10^7	129×512	2.7×10^{-3}	0.07	0.97	0.84	1.09
9	10^{-5}	1×10^8	129×554	5.8×10^{-3}	0.13	0.99	0.73	1.16
10	10^{-5}	1.3×10^8	129×597	7.5×10^{-3}	0.15	0.99	0.67	1.15
11	10^{-5}	1.5×10^8	129×597	8.5×10^{-3}	0.15	0.99	0.64	1.15
12	10^{-5}	1.8×10^8	129×597	1.0×10^{-2}	0.17	0.99	0.61	1.16
13	10^{-5}	2×10^8	161×597	1.1×10^{-2}	0.17	0.99	0.59	1.15
14	10^{-5}	5×10^8	193×682	2.2×10^{-2}	0.24	0.99	0.48	1.18
15	10^{-5}	1×10^9	257×853	3.6×10^{-2}	0.26	0.99	0.41	1.18
16	10^{-5}	2×10^9	321×1024	5.4×10^{-2}	0.20	0.98	0.37	1.14
17	10^{-4}	5×10^6	97×256	1.9×10^{-2}	0.05	0.95	0.66	0.98
18	10^{-4}	1×10^7	97×256	3.4×10^{-2}	0.05	0.93	0.51	0.94
19	10^{-4}	3×10^7	97×256	7.1×10^{-2}	0.03	0.86	0.39	0.95
20	10^{-4}	1×10^8	193×512	1.4×10^{-1}	0.02	0.75	0.32	0.93
21	10^{-4}	3×10^8	257×618	2.6×10^{-1}	0.04	0.77	0.29	0.93

where the contribution of the axisymmetric mode ($m = 0$) is excluded. Qualitatively, the residual energy represents a wealth of waves, eddies, and convective instabilities, while the zonal energy pertains to large-scale axisymmetric features, commonly referred to as jets.

Another key feature of rotating turbulence is the nearly axial flow invariance along the rotation axis $\mathbf{e}_z$, known as flow geostrophy. The geostrophic flow $\mathbf{u}^g$ is obtained by averaging the velocity along the z-direction over the spherical fluid depth following

$$\mathbf{u}^g(s,\phi) = \frac{1}{h^+(s) - h^-(s)} \int_{h^-(s)}^{h^+(s)} \mathbf{u}(s,\phi,z)\mathrm{d}z, \tag{7}$$

where (s,ϕ,z) are the standard cylindrical coordinates. In the above expression, $h^+(s) = -h^-(s) = \sqrt{r_o^2 - s^2}$ if $s \geq r_i$, while $h^-(s) = \sqrt{r_i^2 - s^2}$ and $h^+(s) = \sqrt{r_o^2 - s^2}$ if $s < r_i$. The separation between these two branches marks the location of the so-called tangent cylinder, the imaginary cylinder that circumscribes the inner boundary of the domain and is parallel to $\mathbf{e}_z$. The fluid depth $h(s)$ is defined as

$$h(s) = h^+(s) - h^-(s). \tag{8}$$

For the sake of simplicity, geostrophic velocities inside the tangent cylinder are computed in the Northern hemisphere only. Following the same procedure with $\mathbf{u}^g$ than with $\mathbf{u}$, we compute the geostrophic component of the total, zonal and residual kinetic energy denoted as E_T^g, E_Z^g, E_R^g. Table 1 features the total Rossby number Ro and the energy ratios E_Z/E_T, E_Z^g/E_Z, E_R^g/E_R for the 21 simulations performed in this study.

Last but not least, an estimate of the energetic forcing in the spherical convective shell is given by the mean buoyancy power averaged over the volume P,

$$P = \frac{RaE^2}{Pr} \overline{\langle g u_r T \rangle}, \tag{9}$$

that corresponds to the energy flux injected in the fluid layer by convective instabilities.

3. Results

3.1. Global properties and flow visualization

Fig. 3 shows energy ratios as a function of the global Rossby number Ro across our series of 21 numerical simulations. As previously shown by Christensen (2002) and Yadav et al. (2016), the ratio of the zonal to total kinetic energy E_Z/E_T at a given Ekman number, follows a bell-shaped function where the maximum value increases with decreasing Ekman numbers (Fig. 3a). For $E = 10^{-6}$ the fraction of zonal energy reaches up to $\sim$ 50% of the total energy, a value significantly smaller than the ratio attained in the numerical models with stress-free boundaries (see Yadav et al., 2016, their Fig. 3). When the Rossby number is low, it is associated with decreased Rayleigh numbers, causing the convective motions to approach a weakly nonlinear regime, which is less effective in driving vigorous flows. On the contrary, at the largest Ro, a regime of intense convection is achieved, and residual energy dominates over its zonal counterpart. The bell-shaped pattern of the energy ratio E_Z/E_T is also evident in Fig. 3a for simulations with $E = 10^{-5}$. However, in these simulations, the maximum fraction of zonal energy does not exceed $\sim$ 26% of the total energy. Ultimately, simulations conducted with the largest Ekman number ($E = 10^{-4}$) are strongly dominated by turbulent fluctuations, with E_Z/E_T that remains below 10%. For this Ekman number, viscous effects play a too significant role and preclude the formation of strong zonal jets.

We also show in Figs. 3(b–c) the degree of geostrophy of the zonal and residual flows. The ratio E_Z^g/E_Z indicates that the zonal flow is almost purely geostrophic for $Ro < 10^{-2}$ (Fig. 3b). On the contrary, the ratio E_R^g/E_R continuously decreases with increasing Ro. Consequently, the residual flow is partly geostrophic, and when $Ro > 10^{-2}$, half of its kinetic energy is non-geostrophic.

To illustrate the diversity of our numerical simulations, we now show in Fig. 4 equatorial, meridional and radial cuts of the dimensionless azimuthal velocity u_ϕ, that correspond to snapshots extracted from three selected cases at $E = 10^{-6}$ and one case at $E = 10^{-5}$. The filled-in symbols in Fig. 3 mark their location in terms of energy ratios. In all four images the flow is split into two dynamical regions, separated by the tangent cylinder: a polar region (inside the tangent cylinder) which is dominated by the formation of small-scale convective plumes, and an equatorial region (outside the tangent cylinder) which features azimuthally-elongated structures that correspond to prograde (in red) and retrograde (in blue) zonal jets. To better characterize this multiple jets system, we also report in Fig. 5 the time and azimuthal averages of u_ϕ in the meridional plane. If the jets are essentially confined outside the tangent cylinder (i.e. in the equatorial region), Fig. 5 reveals that increasing the Rossby number tends to enlarge their size and enable the formation of low-latitude jets inside the tangent cylinder. Interestingly, Fig. 4b also reveals the presence of large-scale chevron patterns in the

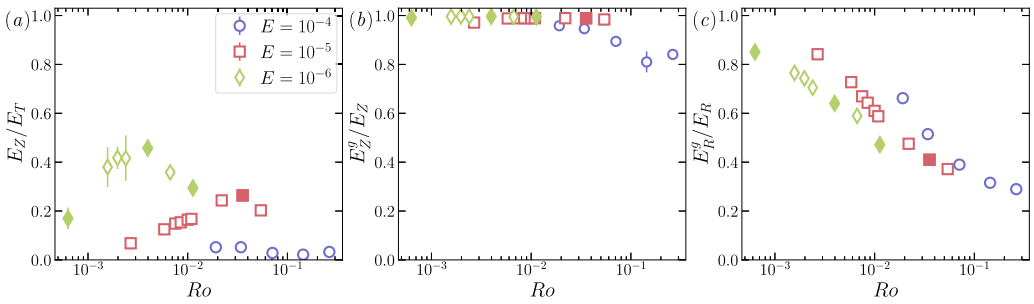

Fig. 3. (*a*) Ratio of zonal to total kinetic energy as a function of the Rossby number *Ro*. (*b*) Ratio of zonal geostrophic kinetic energy to zonal kinetic energy as a function of *Ro*. (*c*) Ratio of residual geostrophic kinetic energy to residual kinetic energy as a function of *Ro*. The error bars correspond to one standard deviation about the time-averaged values. They are smaller than the symbol size for most numerical models. The filled-in symbols correspond to the simulations later highlighted in Figs. 4–6. (For interpretation of the references to colour in this figure legend, the reader is referred to the web version of this article.)

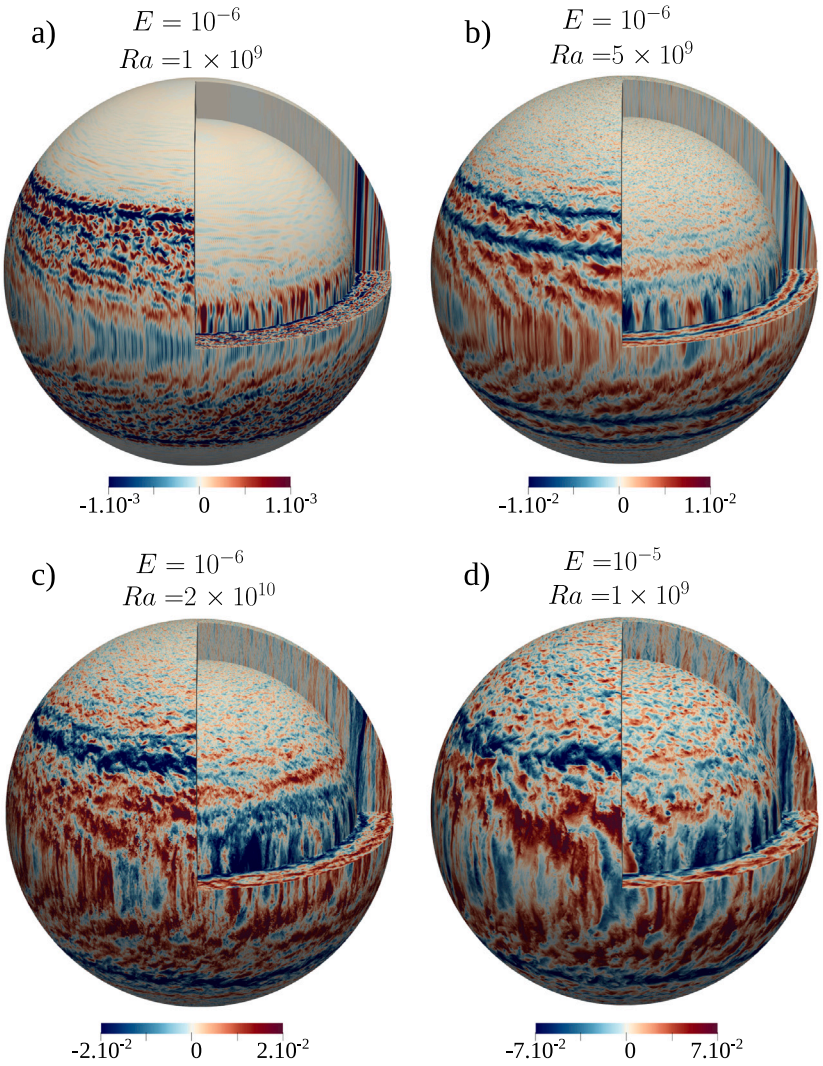

Fig. 4. Instantaneous zonal velocity maps in units of Rossby number, at $r = 4.98$ for the outermost spherical surface and $r = 4.05$ for the innermost one. The horizontal cut corresponds to the equatorial plane. Panels a–d correspond to simulations 1, 5, 7 and 15 in Table 1.

equatorial region. Such patterns are reminiscent of planetary Rossby waves detected in the Sun (Gizon et al., 2021) and further characterized in a numerical model of solar-like rotating convection (Bekki et al., 2022). As shown in Fig. 4b, Simulation 5, in which zonal and residual energy are almost in equipartition, provides a perfect illustration of the coexistence of a prograde equatorial jet and an embedded large-scale wave. These features are less clear in the other simulations where zonal flows never account for more than 30% of the total energy.

To further illustrate the degree of geostrophy of the different flow components and the regionalization of the dynamics, Fig. 6 shows a comparison between u_r and u_ϕ in the equatorial plane (lower halves) with their geostrophic counterparts (upper halves). Increasing the convective forcing at a given Ekman number (panels a to c) goes along with broader jets and larger-scale convective features outside the tangent cylinder. While there is hardly any convective flow inside the tangent cylinder at $Ra = 10^9$ indicating sub-critical polar convection (Gastine

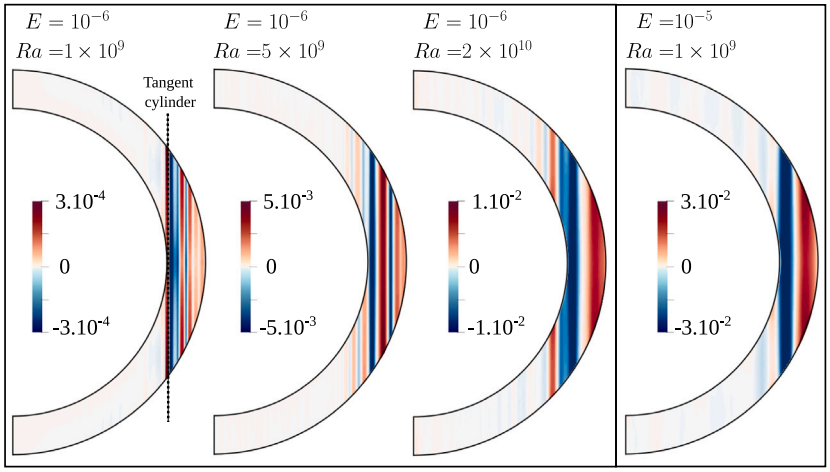

Fig. 5. Time and azimuthal average of the azimuthal velocity in units of Rossby number, for the four simulations shown in Fig. 4.

and Aurnou, 2023), the differences in flow amplitude gradually taper off at large supercriticalities ($Ra \approx 150\, Ra_C$ in both cases shown in panels c and d). The comparison of equatorial and geostrophic flows reveals that the geostrophic averaging mostly implies smoothing out the small-scale eddies while preserving the large scale structures (for a similar analysis in geodynamo models, see Fig. 5 in Schwaiger et al., 2021). As already shown in Fig. 3c, the global ageostrophic residual flow contributions grow with the Rossby number, which translates into increased differences between equatorial and geostrophic flows from panel a to panel d.

As a preliminary conclusion, a general picture of our simulations is that thermal convection, in a rotating spherical shell subjected to rigid mechanical boundaries, tends to spontaneously develop powerful multiple geostrophic zonal flows of alternated directions (for other examples see also Guervilly and Cardin, 2017; Barrois et al., 2022; Gastine and Aurnou, 2023). This trend becomes more pronounced as the Rossby and Ekman numbers are reduced. However, within the range of parameters achieved in the present study, the residual energy remains the predominant component of the flow, at the expense of the zonal energy. Reaching a configuration where the zonal energy prevails over the residuals would necessitate Ekman numbers lower by at least one order of magnitude, presently out of reach to 3D computations if one wishes to conduct a systematic parameter survey.

3.2. Statistical analysis

As stated in the introduction, the theoretical framework of zonostrophic turbulence was developed to study 2D rotating flows in the presence of a β-effect. It has recently been applied to mechanically driven laboratory flows, shallow-water numerical experiments and atmospheric observations. Here, we aim to extend its applicability to 3D convection in a rotating spherical shell. Consequently, a spectral analysis of the flow is in order.

3.2.1. Theoretical energy spectra

In order to account for the zonal anisotropy of the flow, the framework of zonostrophic turbulence defines a zonal spectrum and a residual spectrum in the following universal form Sukoriansky et al. (2002), Galperin et al. (2010),

$$E_R(k) = C_R \Pi^{2/3} k^{-5/3}, \tag{10a}$$

$$E_Z(k_s) = C_Z \beta^2 k_s^{-5}. \tag{10b}$$

The residual spectrum (10a) closely follows the classical Kolmogorov–Batchelor–Kraichnan (KBK) theory of 2D isotropic turbulence, where k is the total wavenumber, $C_R \sim 5-6$ is taken to be a universal constant and Π is the energy transfer rate between the different scales of motions (Boffetta and Ecke, 2012). The zonal spectrum (10b) characterizes the axisymmetric energy and is measured along wavenumbers k_s in the direction orthogonal to the zonal flow. C_Z is assumed to be a universal constant of order unity, whose value was shown to lie around 0.5 in numerical simulations on the sphere (Sukoriansky et al., 2002, 2007), around 2 for Jupiter (Galperin et al., 2014), and in the range $0.3 - 2.7$ for the laboratory experiments described in Cabanes et al. (2017) and Lemasquerier et al. (2023). The β parameter represents the latitudinal gradient of planetary vorticity. In 2D spherical flows, it directly stems from the variation of the Coriolis parameter with the colatitude θ and can be expressed as $\beta = 2\Omega|\sin\theta|/r_o$. In 3D spherical shells, β arises from the variations of the fluid layer depth with the cylindrical radius s and is commonly referred to as the topographic-β (e.g. Heimpel and Aurnou, 2007). It is then expressed by

$$\beta(s) = \frac{2\Omega}{h}\frac{\mathrm{d}h}{\mathrm{d}s}, \tag{11}$$

with $h(s)$ the fluid depth defined in Eq. (8). To compare theoretical predictions with the velocity fields obtained from numerical simulations, it is necessary to conduct a spectral decomposition of the flow.

3.2.2. Spectral flow decomposition

Given the spherical geometry of our numerical setup, spherical harmonic functions could spontaneously be invoked to compute energy spectra along the θ and ϕ directions (see for example Boer, 1983; Böning et al., 2023). However, rotationally-constrained flows show a pronounced invariance along the axis of rotation, as shown in Figs. 4 and 5. In such flows, dominant features are cylindrical in nature, which favours Bessel–Fourier basis functions for spectral analysis in the s and ϕ directions, respectively. This choice impacts the typical scales that emerge from the spectral decomposition. As an illustrative example, when a velocity field is projected onto the spherical surface, the equatorial jet appears significantly larger in comparison to the jets at higher latitudes (see Fig. 4). However, when observed along the cylindrical radial direction (as shown in the meridional cross-sections in Fig. 5), all jets appear to have the same width, which allows in turn to unambiguously relate a wavenumber with a lengthscale.

To carry out a spectral flow decomposition in cylindrical geometry, we make use of two distinct velocity fields: the geostrophic velocity projected onto a disc (see Eq. (7)), and the velocity on the equatorial annulus at $\theta = \pi/2$ (see the equatorial cut in Fig. 4). As detailed in Section 2.3, the geostrophic velocity is defined on the disc, at all cylindrical radii, by averaging along $\mathbf{e}_z$, while the equatorial velocity is only defined on the annulus outside the tangent cylinder. In both cases, the domain is periodic in ϕ and is finite in radius, with $s \in [a, b]$, say.

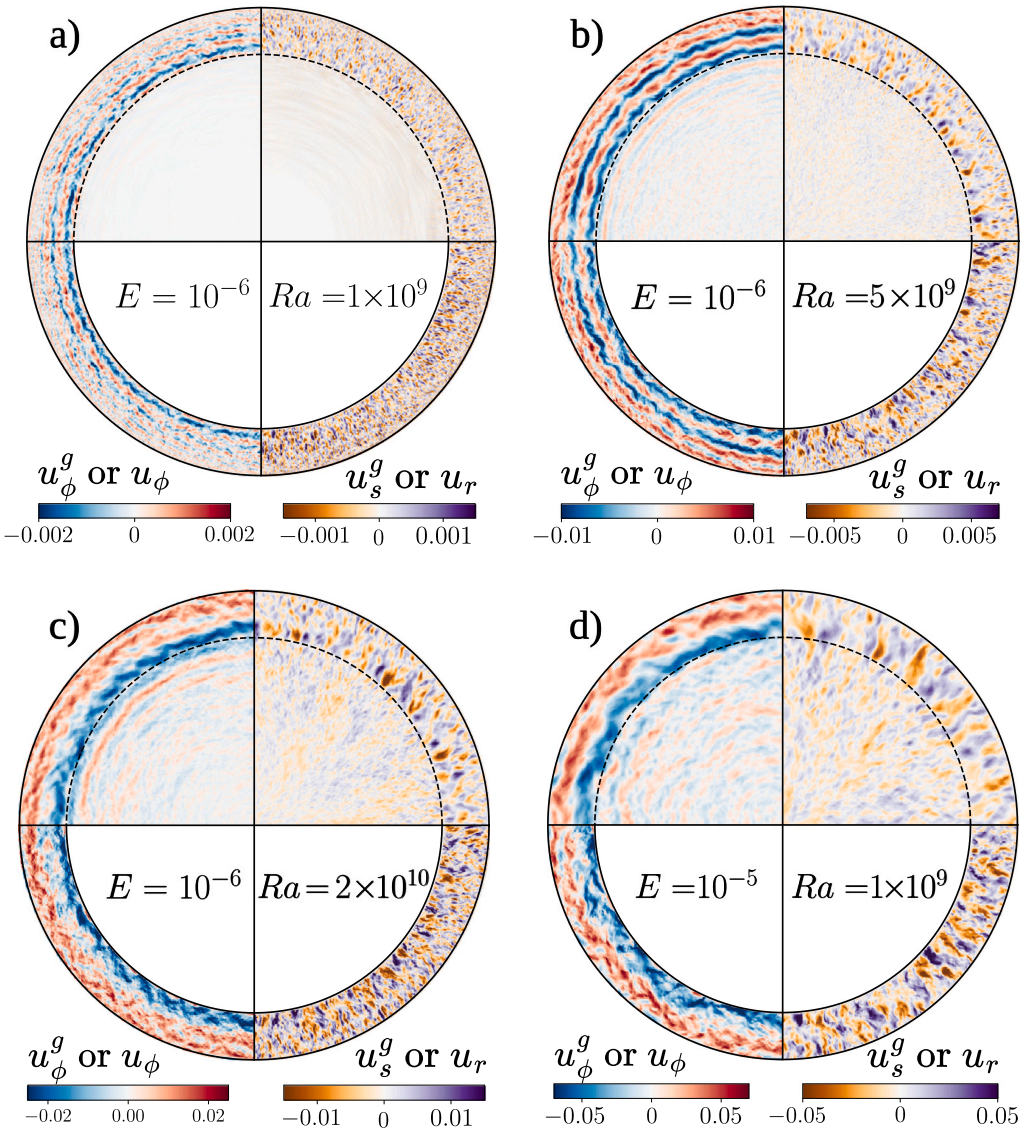

Fig. 6. Snapshots of different flow components for the four simulations shown in Figs. 4 and 5. For each panel, the upper half corresponds to the geostrophic flow components with u_ϕ^g on the left and u_s^g on the right, while the bottom half corresponds to the flow in the equatorial plane with $u_\phi(\theta = \pi/2)$ on the left and $u_r(\theta = \pi/2)$ on the right. The dashed arcs in the upper halves mark the location of the tangent cylinder.

Following Wordsworth et al. (2008) and Lemasquerier et al. (2023), one can then decompose any field $f(s,\phi)$ defined over such a domain into spectral coefficients using Bessel–Fourier transforms,

$$\hat{\hat{f}}_{mn} = \int_a^b \int_0^{2\pi} f(s,\phi)\Psi_{mn}(s)e^{-im\phi} s \, \mathrm{d}s \, \mathrm{d}\phi, \tag{12}$$

with m and n the azimuthal and radial dimensionless wavenumbers, respectively (for a review of different spectral decompositions on the disc, see Boyd and Yu, 2011).

On the disc, the integral along the cylindrical radius s is defined over the interval $[0, r_o]$, and $\Psi_{mn}(s) \equiv J_m(\alpha_{mn}s)$, where J_m denotes the Bessel function of the first kind of order m. For a disc subjected to a Dirichlet boundary condition (e.g. Sneddon, 1946), the wavenumbers α_{mn} are the roots of the equation

$$J_m(\alpha_{mn}r_o) = 0\,. \tag{13a}$$

The radial wavenumbers $k_{mn} = \alpha_{mn}$ take discrete values since the domain is bounded (see for example Wang et al., 2009). This spectral decomposition defines the Hankel transform on the disc (e.g. Baddour, 2019).

On the annulus $s \in [r_i, r_o]$, the support functions consist of a linear combination of Bessel functions of the first and second kind (MacRobert, 1932) J_m and Y_m such that

$$\Psi_{mn}(s) \equiv Y_m(\alpha_{mn}r_o)J_m(\alpha_{mn}s) - J_m(\alpha_{mn}r_o)Y_m(\alpha_{mn}s)\,. \tag{14}$$

When Dirichlet boundary conditions are enforced on both sides, the wavenumbers α_{mn} are the roots of Cinelli (1965)

$$Y_m(\alpha_{mn}r_i)J_m(\alpha_{mn}r_o) - J_m(\alpha_{mn}r_i)Y_m(\alpha_{mn}r_o) = 0\,. \tag{15}$$

For this combination of geometry and boundary conditions, Eq. (12) is then known as the Weber–Orr transform.

We compute kinetic energy spectra following

$$E_{mn} = \frac{r_o}{2V^\star} N_{mn} \left(|\mathcal{U}_{mn}|^2 + |\mathcal{V}_{mn}|^2 \right), \tag{16}$$

where $\mathcal{U}_{mn} \equiv \widehat{\sqrt{h}\hat{u}_s}$ and $\mathcal{V}_{mn} \equiv \widehat{\sqrt{h}\hat{u}_\phi}$ to account for the height variation of the fluid depth h defined in Eq. (8). Note that a single hat $\hat{\cdot}$ corresponds to a Fourier transform, while two hats correspond to a Bessel–Fourier transform. In the above equation, $V^\star$ either corresponds to the full fluid volume in the case of the disc ($V^\star = V$) or to the volume outside the tangent cylinder only in the case of the annulus ($V^\star = V^a =$

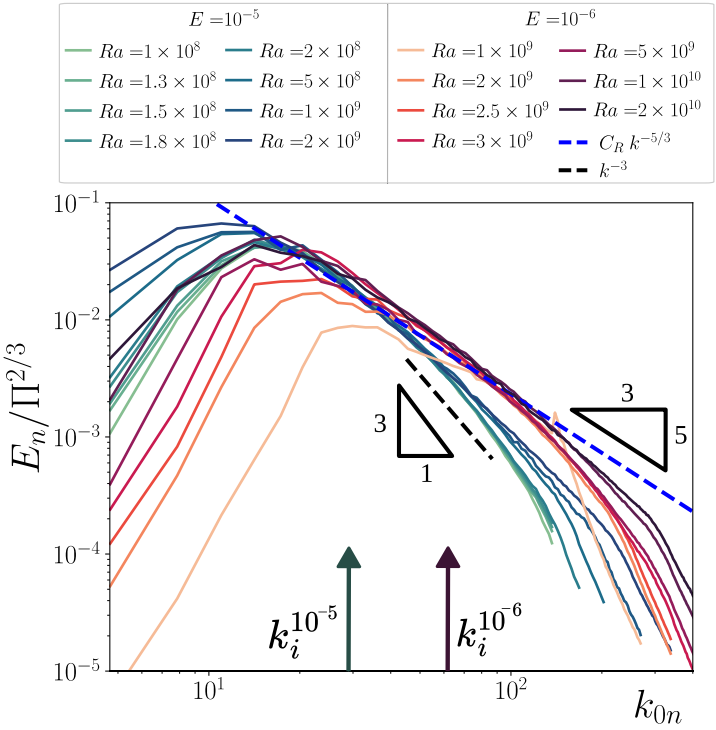

Fig. 7. Residual spectra of the equatorial velocity on the equatorial annulus. The vertical arrows correspond to the two injection wavenumbers k_i^E for $E = 10^{-5}$ and $E = 10^{-6}$. Green to blue colour gradient goes from $Ra = 10^8$ to 2×10^9 for simulations at $E = 10^{-5}$. Light orange to purple colour gradient goes from $Ra = 10^9$ to 2×10^{10} for simulations at $E = 10^{-6}$. The theoretical prediction of the residual spectra from Eq. (10a) corresponds to the dashed blue line using $C_R = 5$. The dashed black line corresponds to a k_{0n}^{-3} slope. (For interpretation of the references to colour in this figure legend, the reader is referred to the web version of this article.)

$(4\pi/3)[h^+(r_i)]^3$). In the above expression, N_{mn} is a normalization factor which depends upon the relevant Bessel–Fourier transform such that

$$N_{mn} = \frac{2\pi}{r_o^2} \frac{1}{J_{m+1}^2(\alpha_{mn} r_o)} \tag{17}$$

for the disc (see Sneddon, 1946; Guizar-Sicairos and Gutiérrez-Vega, 2004; Baddour, 2019), and

$$N_{mn} = \frac{\pi^3 \alpha_{mn}^2 J_m^2(\alpha_{mn} r_o)}{J_m^2(\alpha_{mn} r_i) - Y_m^2(\alpha_{mn} r_o)} \tag{18}$$

for the annulus (Sneddon, 1946; Cinelli, 1965).

We distinguish the zonal spectrum $E_Z(k_{0n}) = E_{0n}$ that contains the kinetic energy of the azimuthal mode $m = 0$ and the residual spectrum $E_R(k_{0n}) = \sum_{m=-\ell_{\max}, m\neq 0}^{\ell_{\max}} E_{mn}$, which is the contribution of all non-zonal modes, $m \neq 0$. In this spectral analysis, each mode m has different wavenumbers $k_{mn} = \alpha_{mn}$ and the associated zonal wavenumbers are $k_{0n} = \alpha_{0n}$. As suggested by Lemasquerier et al. (2023) we perform a summation into spectral bins for modes $m \neq 0$ in order to compute the residual spectrum. The spectral bins dk are defined to correspond to the zonal wavevector k_{0n}. Here, we consider that any typical length scale is half a period in radius and can be computed using $L = \pi/k_{mn}$. Hereafter, all spectra are computed once the steady state is achieved in our simulations and a time average over at least 20 statistically independent spectra is computed.

3.2.3. Residual spectra

Fig. 7 shows the residual energy spectra computed from the equatorial velocity on the annulus and for the entire set of simulations at $E = 10^{-5}$ and 10^{-6}. At a given Ekman number, the injection scale is estimated by $k_i^E = m_c/r_i$ using the critical azimuthal wavenumber at onset of convection m_c computed by Barik et al. (2023), which give $m_c = 116$ and 247 for $E = 10^{-5}$ and 10^{-6}, respectively. Once the statistically-steady state has been reached, $\Pi = P$ (Eq. (9)), providing an effective way to measure the energy transfer rate in convection driven turbulence. This enables a straightforward comparison of the residual spectra for different convective forcings by considering $E_R(k)/P^{2/3}$. All residual spectra are then found to follow the $-5/3$ slope expected from the KBK theory of 2D-turbulence, with $C_R \approx 5$ in Eq. (10a).

This also shows that when the Rayleigh number increases and the Ekman number decreases, the range of scales where the $-5/3$ scaling applies increases, with larger wavenumbers exhibiting a slope near -3. This change in the spectral slope occurs at wavenumbers close to the injection scale k_i^E. Such flow properties are reminiscent of the paradigm of 2D-turbulence coined by Kraichnan (1967): an inverse cascade of kinetic energy from injection to large scales with a $-5/3$ slope, and a direct cascade of enstrophy to small scales with a -3 slope (see Deusebio et al. 2014 and Boffetta and Ecke 2012 for a review). Fig. 7 illustrates that lowering the Ekman number goes along with a broadening of the range of scales that adhere to the $-5/3$ slope towards small wavenumbers, possibly suggesting a more effective inverse cascade. Recently, Böning et al. (2023) showed that a $-5/3$ slope can also be found in spherical convective flows, where zonal jets are driven by statistical correlations of small convective scales instead of the inverse turbulent cascade invoked in the theory of 2D-turbulence. To differentiate between these two mechanisms and determine which one is at play in our numerical simulations, a more detailed analysis of energy and enstrophy transfers would be necessary, an analysis that goes beyond the scope of the current study.

In Fig. 8a, we expand our statistical analysis by displaying three distinct residual spectra computed from simulation 5, which corresponds to the maximum energy ratio $E_Z/E_T = 0.5$ and the control parameters $E = 10^{-6}$ and $Ra = 5 \times 10^9$. In this analysis, we concurrently display the residual spectra computed on the annulus, originating from both the equatorial (pink) and geostrophic (light pink) velocities, along with the spectrum computed on the disc from the geostrophic velocity (black). The light pink and black curves illustrate a decrease in the magnitude of the residual spectra for the geostrophic velocity when compared to the equatorial velocity. This reduction becomes even more pronounced when we consider a spectral decomposition on the disc

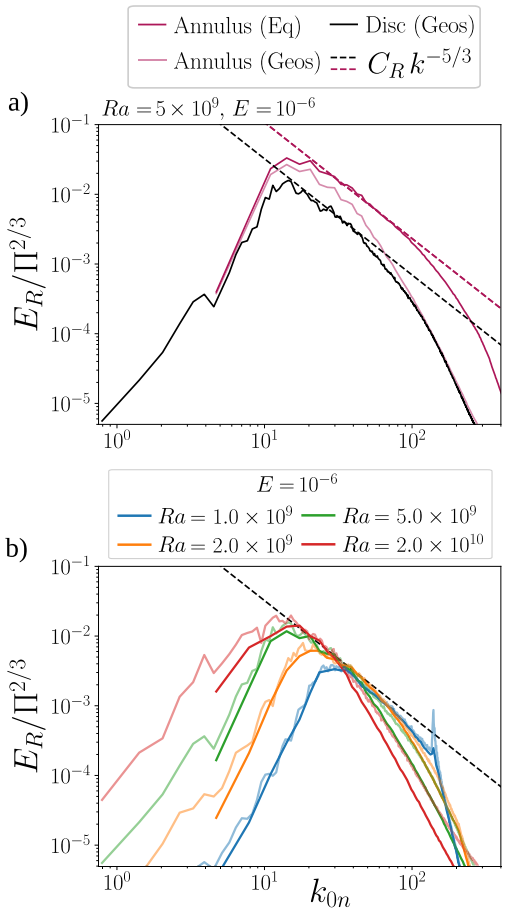

Fig. 8. (*a*) Residual spectra of simulation 5, computed for the geostrophic (geos) and equatorial (Eq) velocities on the annulus as well as for the geostrophic velocity on the disc. The pink curve is the same as the one presented in Fig. 7. (*b*) Comparison of the residual spectra computed on the disc (light lines) and on the annulus (opaque lines) for the geostrophic residual velocity for four selected simulations at $E = 10^{-6}$ with increasing supercriticalities. To stress the influence of the geometric factor, the residual spectra on the annulus have been multiplied by V^a/V. On both panels, the dashed pink and black lines are theoretical predictions from Eq. (10a) with $C_R = 5$ and 1.5 respectively. (For interpretation of the references to colour in this figure legend, the reader is referred to the web version of this article.)

rather than on the annulus. It is evident that part of this reduction results from the axial averaging involved in the computation of the geostrophic component. Referring to Fig. 3, we can recall that only 64% of the residual energy is attributed to the geostrophic component for simulation 5 (see also Table 1). However, the magnitude of the energy spectrum on the disc is further reduced compared to that on the annulus. This reduction can be attributed to the presence of the tangent cylinder, which forms a dynamical barrier leading to different regionalized dynamics between high and low latitude regions (e.g. Gastine and Aurnou, 2023).

These different regions manifest as a consequence of the inherent anisotropy of the convective forcing. Dormy et al. (2004) demonstrated that the onset of convective instabilities in a rotating spherical shell is localized adjacent to, but outside, the tangent cylinder. Additionally, imposing no-slip boundary conditions in our numerical setup further reinforces the existence of these two dynamical regions, suppressing the formation of large-scale flows within the polar region. The combination of these effects results in significant heterogeneities in turbulent mixing throughout the fluid shell. Consequently, when incorporating the weakly convective polar region into the spectral decomposition on the disc, there is a marked reduction in the residual spectrum. This decrease can hence be attributed to the combined effects of partial flow geostrophy and differences of flow amplitude inside and outside the tangent cylinder. The latter can be approximated by a geometric factor $V/V^a \approx 2.2$ in the limit of sub-critical convection inside the tangent cylinder. To account for those effects, we fit the black residual spectrum in Fig. 8a using Eq. (10a) by lowering the residual constant from $C_R = 5$ to 1.5 (as indicated by the black dashed line). This shows that within spherical shell convection, the residual spectra cannot be uniquely described by the theory of 2D isotropic, homogeneous, turbulence that arises in unconstrained turbulent environments (Kraichnan, 1967). Instead, the polar and equatorial dynamical regions, when considered separately, are nearly homogeneous and must be treated accordingly. This approach is illustrated in our consideration of the equatorial region alone in Fig. 7.

Considering the parameter range for icy satellites, where $10^{-12} \lesssim E \lesssim 10^{-10}$ and $10^{16} \lesssim Ra \lesssim 10^{24}$, it is plausible that the formation of zonal jets extends to higher latitudes. Such a dynamical configuration could lead to a more homogeneous distribution of turbulence throughout the fluid volume, causing the spectrum computed on the disc to converge towards that computed on the annulus. To test this hypothesis, we present in Fig. 8b residual spectra obtained for a range of simulations with increasing convective forcings from $Ra = 10^9$ (Simulation 1) to $Ra = 2 \times 10^{10}$ (Simulation 7). To highlight the flow regionalization, the residual spectra on the annulus have been multiplied by the aforementioned geometric factor V^a/V. While a nearly perfect overlap is observed for both spectra (i.e. on the disc and the annulus) in the weakly-forced case (blue lines), they gradually depart from each other as supercriticality increases. This deviation is more sizeable at larger scales ($k_{0n} \leq 10$), particularly for the highly turbulent case $Ra = 2 \times 10^{10}$ (red lines). This reflects a growing fraction of energy inside the tangent cylinder, as also illustrated in Fig. 6. Nonetheless, the parameters covered in this study do not allow to reach comparable energy levels inside and outside the tangent cylinder. Would this homogenization process becomes complete within the parameter range relevant to icy satellites, one can speculate that a spectral analysis on both the disc and the annulus would yield the same result, within the geometric factor V^a/V involved in Fig. 8b.

3.2.4. Zonal spectra

Fig. 9 shows zonal energy spectra computed from the geostrophic velocity on the annulus and on the disc. We have selected energy spectra from different simulations at $E = 10^{-6}$ and 10^{-5}, including different Rayleigh numbers. For all the numerical simulations, the zonal spectra consistently exhibit a -5 slope on approximately two decades and the energetic amplitude is well predicted by Eq. (10b). The dimensionless β parameter is estimated at the mean radius of the equatorial annulus $s_{\rm mid}$,

$$\beta = \frac{2 s_{\rm mid}}{r_o^2 - s_{\rm mid}^2} \quad \text{with} \quad s_{\rm mid} = \frac{1}{2}(r_i + r_o), \tag{19}$$

and the zonal constant which best fits the spectra is $C_Z = 0.5$. We opt for estimating β at the mean equatorial radius because it corresponds to the average position of the zonal jets since they are mostly confined outside the tangent cylinder (see Fig. 5). This condition generally holds for all simulations, where only weak zonal jets form in the polar region. However, our estimate of β may require reconsideration if zonal jets were to extend towards the poles. This is the case for instance in the simulations with free-slip boundary conditions conducted by Soderlund et al. (2014) or possibly in the range of parameters expected for the icy satellites. In such configurations, the β parameter would need to be estimated differently to account for high latitudes. On the other hand, we estimate the zonal constant $C_Z = 0.5$ by fitting the magnitude of the zonal spectra computed on the annulus rather than on the disc. Again, the reason for this choice is that the disc encompasses fluid regions with very heterogeneous flows. In addition, the spherical shell geometry has its own spectral signature which exhibits energetic

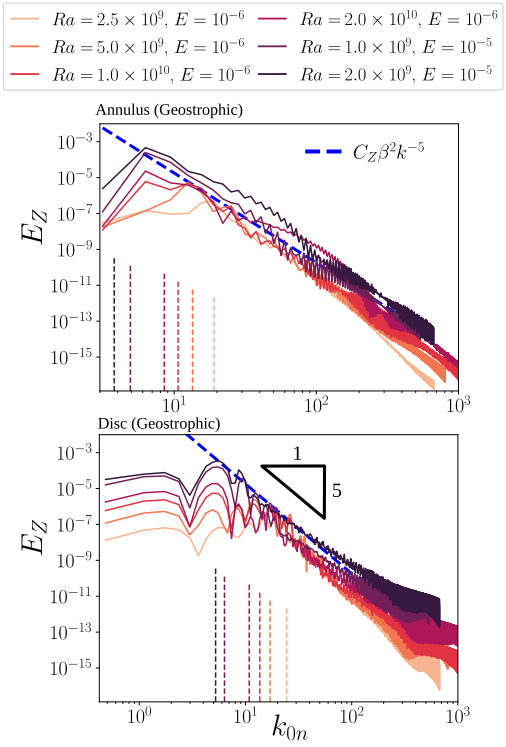

Fig. 9. Zonal spectra of the geostrophic velocity computed on the annulus (top panel) and on the disc (bottom panel). The theoretical prediction of the zonal spectra from Eq. (10b) corresponds to the dashed blue line using $C_Z = 0.5$. Vertical dashed segments are Rhines wavenumbers k_{Rh} from Eq. (20) and for each simulation. (For interpretation of the references to colour in this figure legend, the reader is referred to the web version of this article.)

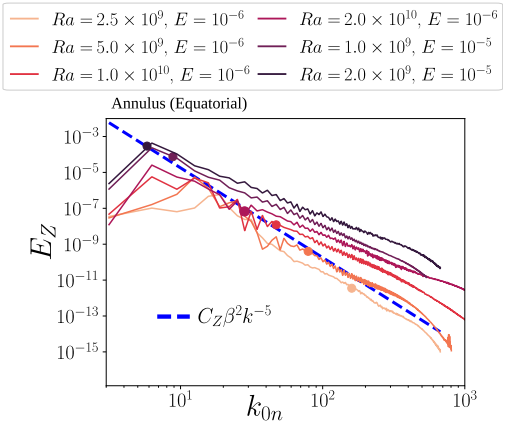

Fig. 10. Zonal spectra of the equatorial velocity computed on the annulus. The theoretical prediction of the zonal spectra from Eq. (10b) corresponds to the dashed blue line using $C_Z = 0.5$. Dots are Rossby scales k_{Ro} from Eq. (21). (For interpretation of the references to colour in this figure legend, the reader is referred to the web version of this article.)

bumps at intermediate wavenumbers when using Bessel–Fourier decomposition (see Fig. 9). These bumps arise because the flow adopts the cylindrical geometry of the fluid shell (one equatorial region with strong jets, the other without), which artificially affects the energy spectra. This would probably not occur if jets would have formed at all cylindrical radii, making the spectral decomposition on the disc more relevant. This configuration may occur in the parameter range relevant to icy satellites, or it can equally arise in simulations with free-slip boundary conditions, where significant polar and equatorial zonal flows are known to develop (as observed in simulations by Soderlund, 2019; Böning et al., 2023). Conducting a spectral analysis of these free-slip simulations could provide further insights into the dynamics of such flows and their spectral distribution.

It is worth noting that the zonal constant C_Z obtained here lies within the range of values $0.3 \lesssim C_Z \lesssim 2.7$ estimated in previous studies of zonostrophic turbulence (Sukoriansky et al., 2002; Galperin et al., 2014; Cabanes et al., 2017; Lemasquerier et al., 2023). We thus reinforce its universality by extending it to deep-seated convective flows. Furthermore, a key implication of Eq. (10b) is that the energetic amplitude of the zonal spectra is independent of the convective forcing and solely depends on the rotation rate Ω and some geometric parameters given in Eq. (19).

It is also well accepted that in flows with a strong β-effect, the Rhines scale (Rhines, 1975) is a good approximation of the frictional scale denoted by k_f in Fig. 2. This scale is pivotal in arresting the inverse cascade of energy in such flows (e.g. Sukoriansky et al., 2007); it is defined by

$$k_{Rh} = \sqrt{\frac{\beta}{2U_g}}. \tag{20}$$

where U_g is the root-mean-square geostrophic velocity integrated either on the disc or on the annulus. The dashed vertical segments in Fig. 9 show that the Rhines wavenumber matches quite effectively with the most energetic scale, above which the energy systematically decreases. The associated Rhines scale $L_{Rh} = \pi/k_{Rh}$ has also proved to be a good estimate of the typical jets width (see Heimpel and Aurnou, 2007; Gastine et al., 2014; Bire et al., 2022, for examples in spherical rotating convection). Since the jets size increases with the Rayleigh number (see Figs. 5 and 6 for an illustration) it results in zonal spectra which further extend towards smaller wavenumbers. At the highest Rayleigh numbers, the energy maxima reach typical length scales corresponding to almost half the shell gap. As previously stated, these length scales cannot be clearly identified in zonal spectra computed on the disc because of the zonal flow regionalization.

Finally, we apply the zonostrophic theory to zonal energy spectra obtained from the equatorial velocity on the annulus, as shown in Fig. 10. Similarly to the geostrophic component, zonal energy at small wavenumbers are well accounted for by Eq. (10b). However, for large wavenumbers, the zonal energy of the equatorial flow shows a strong dependence on the convective forcing, since its magnitude increases with increasing Rayleigh numbers. The slope also departs from the -5 scaling and gradually tapers off on increasing convective forcings. In order to estimate the typical wavenumber at which the zonal spectra deviate from the theoretical predictions, we introduce a Rossby wavenumber $Ro_k = Ro\, k_{0n}/\pi$. Assuming an arbitrary threshold value of $Ro_k = 0.1$ to mark the limit of strong rotational constraint (a similar threshold is used in the study by Christensen and Aubert, 2006), we define a critical wavenumber as follows,

$$k_{Ro} = \frac{0.1\pi}{Ro}. \tag{21}$$

For wavenumbers where $k < k_{Ro}$, the flow is strongly geostrophic and characterized by a Rossby number lower than 0.1. These scales are the most energetic, and as a result, global properties presented in Fig. 3 reveal a zonal flow that is predominantly geostrophic. Thus, although the theory of zonostrophic turbulence does not explain the energy distribution of the equatorial velocity at all scales, it gives a good estimate of the zonal energy in the convective flows.

Here, we would like to stress that the zonostrophic theory remains applicable in the transitional regime of rotating convection (Fig. 1), even in setups where the zonal energy represents only a weak fraction of the total kinetic energy (see Table 1). However, a crucial question arises when approaching the non-rotating limit – a condition possibly relevant for Titan, Europa and Ganymede – in which the flow becomes essentially ageostrophic. Although our study reveals that approximately 99% of the zonal energy is geostrophic for all simulations with $E = 10^{-5}$

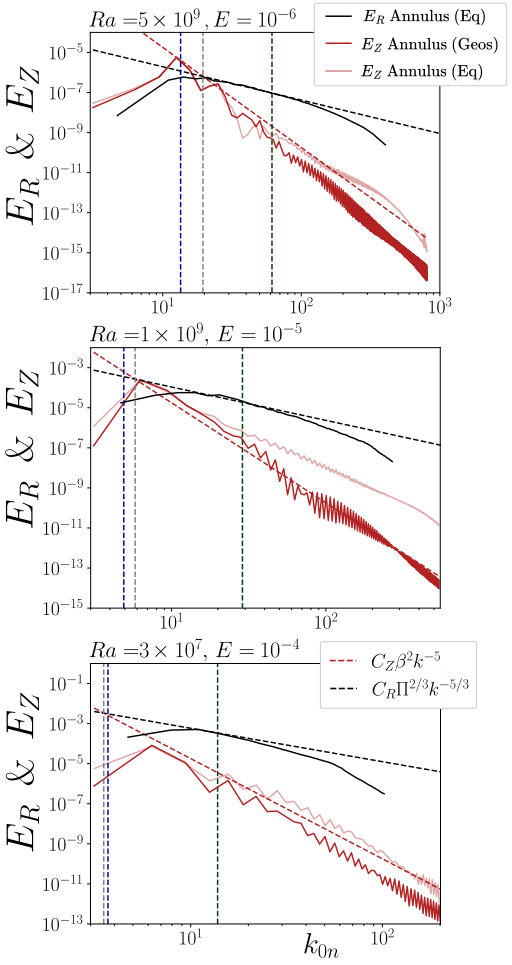

Fig. 11. Zonal and residual energy spectra computed on the annulus from the equatorial (Eq) and geostrophic (Geos) velocities. Panels from top to bottom correspond to simulations 5, 15 and 19 in Table 1. The red and black dashed lines are the theoretical predictions of the zonal and residual spectra using the zonal constant $C_Z = 0.5$ and the residual constant $C_R = 5$. Vertical lines corresponds to Rhines' wavenumber (blue), the transitional wavenumber (grey) and the injection wavenumber $k_i^E = m_c/r_i$ (green), with $m_c = 55$, 116 and 247 for $E = 10^{-4}$, 10^{-5} and 10^{-6}, respectively (Barik et al., 2023). (For interpretation of the references to colour in this figure legend, the reader is referred to the web version of this article.)

and 10^{-6}, it is likely that this fraction decreases when trending towards the non-rotating limit. As the determination of the boundary of the domain where zonostrophic theory applies remains unfortunately inaccessible to present computations, it is difficult to provide a conclusive answer in that regard.

For now, it is crucial to bear in mind that future energetic predictions for subsurface oceans, based on zonostrophic theory, will provide an estimate for the *geostrophic component* of the zonal energy.

3.3. The zonostrophy index

We show in Fig. 11 the zonal and residual spectra for simulations 5, 15 and 19 corresponding to the highest ratio of zonal energy E_Z/E_T for numerical experiments with $E = 10^{-6}$, 10^{-5} and 10^{-4}. The intersection between the theoretical $-5/3$ (Eq. (10a)) and -5 (Eq. (10b)) spectra defines a transitional wavenumber, which can be expressed as

$$k_\beta = \left(\frac{C_Z}{C_R}\right)^{3/10}\left(\frac{\beta^3}{\Pi}\right)^{1/5}. \tag{22}$$

This wavenumber defines the scale at which the theoretical zonal spectrum overcomes the residual one. Thus, the range of wavenumbers $k_{Rh} < k < k_\beta$ is known as the zonostrophic inertial range, in which the zonal jets dominate energetically. In rotating turbulent flows, this inertial range exists if the zonostrophy index $R_\beta = k_\beta/k_{Rh}$ is greater than unity. At $E = 10^{-6}$, the simulation 5 satisfies this condition with $R_\beta = 1.45$ and the zonal spectrum dominates the residual spectrum in the range predicted by the Rhines and transitional wavenumbers. For the simulation 15 at $E = 10^{-5}$, the zonostrophic inertial range is significantly reduced and the intersection of the zonal and residual spectra is poorly predicted by the theory. With an index of $R_\beta = 1.18$, this simulation shows that the β parameter is too weak to efficiently channel energy in the zonal flow component. Finally, simulation 19 at $E = 10^{-4}$ is not in the zonostrophic regime with $R_\beta < 1$ and the residual energy largely dominates its zonal counterpart. The flow is energetically governed by the convective forcing, given that the residual energy is determined by the convective power following Eq. (10a). With a nearly $-5/3$ slope at all wavenumbers, the behaviour of the flow resembles that of 3D-isotropic turbulence, with a forward energy cascade from energy injection at small wavenumber ($k_i^{10^{-4}} \approx 14$) down to viscous dissipation at larger wavenumber. Nonetheless, although the residual energy dominates, the zonal spectrum preserves its -5 slope and magnitude predicted by Eq. (10b). In this simulation, the influence of both large viscosity ($E = 10^{-4}$) and substantial rotational effects ($Ro \sim 0.07$) is evident, leading to 86% of the zonal energy to be in geostrophic balance. Hence, the weak yet mostly geostrophic zonal flows still adhere to the -5 theoretical scaling.

We report in Table 1 the zonostrophy indices for all numerical simulations. The general trend that emerges is that the zonostrophy index increases on decreasing Ekman numbers. This goes along with a greater fraction of zonal energy in the convective shell. Using 2D simulations on a rotating sphere, Galperin et al. (2010) suggest that a lower bound for the zonostrophic regime is rather $R_\beta \simeq 2.5$. They argue that below this value, rotating turbulence occurs in a transitional regime between the dissipation-dominated regime and zonostrophic turbulence. The threshold value of 2.5 is however only indicative and has been established for specific cases of 2D-turbulence (Sukoriansky et al., 2007). Here, in 3D convective flows, with no-slip boundary conditions at the top and bottom of the spherical shell, we never exceed the value of $R_\beta = 1.45$. The laboratory experiments conducted by Lemasquerier et al. (2023) also reveal zonostrophy indices that do not surpass the value of 2. Yet, the theory accurately predicts the spectral energy distribution, even when the residual energy dominates, especially in simulations with $E = 10^{-6}$. Consistently, we argue that zonostrophic turbulence is a relevant framework for analysing convective flows enclosed within a rotating spherical fluid layer. We now propose to use it to make a first theoretical prediction of the typical velocity of subsurface oceans.

4. Implications for subsurface oceans

In order to apply the framework of zonostrophic turbulence to the subsurface oceans of the icy satellites, we assume that this theory can be extrapolated to more extreme parameters, despite the distance between the planetary regimes and those covered by the 3D numerical models (recall Fig. 1). This extrapolation has already proven effective, as (Galperin et al., 2014) successfully applied this theory to *in situ* measurements of the jovian zonal jets collected from the Cassini and Voyager missions. Our goal here is to use Eqs. (10a)–(10b) to generate theoretical residual and zonal spectra and estimate the corresponding velocities for the subsurface oceans of Enceladus, Titan, Europa and Ganymede.

To this end, we present in Table B.3 some properties of the subsurface oceans in dimensional units (extracted from Soderlund, 2019): the thermal expansivity α, the gravitational acceleration g, the heat flux q, the density ρ, the heat capacity C_p, the ocean depth D and the ice thickness D_I. These properties have been obtained in previous studies (see caption in Table 2) by considering different water compositions

Table 2
Water shell structural properties of the icy satellites along with our velocity predictions. The buoyancy power is estimated using Eq. (23). The ocean depths, denoted as D, are derived from the interior model properties provided by Vance et al. (2018) and references therein. The upper bound of the geostrophic zonal velocity $\max(U_z)$ is estimated using Eq. (27). The Rhines scale results from the combination of Eqs. (24) and (27). The residual velocity U_r is determined using Eq. (24) and the values are averaged while considering the uncertainty associated with the zonal constant C_Z. The transitional scale is determined using Eq. (22), taking into account our calculated value of the topographic β parameter following Eq. (19).

	Enceladus	Titan	Europa	Ganymede
		Buoyancy power, P_s (10^{-13} m^2/s^3)		
$MgSO_4$ 10 wt%	0.48, 2.63	3.11, 16.25, 20.69	17.26, 92.17	16.22, 30.11
Seawater	0.04, 0.2	–	18.38, 96.72	–
Water	–	13.54, 25.26, 28.65	14.62, 72.47	14.8, 28.07, 156.26
		Ocean thickness, D (km)		
$MgSO_4$ 10 wt%	13, 63	91, 333, 403	103, 131	287, 493
Seawater	12, 55	–	99, 126	–
Water	–	130, 369, 420	97, 124	119, 361, 518
		Zonal velocity upper bound, $\max(U_z)$ (m s^{-1})		
$MgSO_4$ 10 wt%	0.011, 0.047	0.149, 0.551, 0.666	0.237, 0.599	0.43, 0.715
Seawater	0.003, 0.013	–	0.241, 0.605	–
Water	–	0.355, 0.713, 0.796	0.213, 0.521	0.297, 0.616, 1.66
		Residual velocity, U_r (10^{-3} m s^{-1})		
$MgSO_4$ 10 wt%	1.45, 4.4	9.38, 25.16, 29.07	13.86, 29.93	20.89, 30.37
Seawater	0.48, 1.4	–	14.53, 30.36	–
Water	–	18.72, 31.05, 33.82	12.85, 27.12	16.18, 27.43, 60.71
		Rhines scale, L_{Rh}/D, $C_Z = 0.3$		
$MgSO_4$ 10 wt%	0.4, 0.4	2.1, 2.1, 2.1	1.1, 1.6	1.4, 1.3
Seawater	0.2, 0.2	–	1.2, 1.7	–
Water	–	2.7, 2.3, 2.3	1.1, 1.6	1.7, 1.5, 2.0
		Rhines scale, L_{Rh}/D, $C_Z = 2.7$		
$MgSO_4$ 10 wt%	0.2, 0.2	1.2, 1.2, 1.2	0.6, 0.9	0.8, 0.8
Seawater	0.1, 0.1	–	0.7, 0.9	–
Water	–	1.5, 1.3, 1.3	0.6, 0.9	1.0, 0.8, 1.1
		Transitional scale, L_β/D, $C_Z = 0.3$		
$MgSO_4$ 10 wt%	0.09, 0.07	0.25, 0.21, 0.21	0.14, 0.17	0.14, 0.13
Seawater	0.05, 0.04	–	0.14, 0.18	–
Water	–	0.29, 0.22, 0.22	0.14, 0.17	0.2, 0.14, 0.18
		Transitional scale, L_β/D, $C_Z = 2.7$		
$MgSO_4$ 10 wt%	0.05, 0.04	0.13, 0.11, 0.11	0.07, 0.09	0.07, 0.07
Seawater	0.03, 0.02	–	0.07, 0.09	–
Water	–	0.15, 0.12, 0.11	0.07, 0.09	0.1, 0.07, 0.09

of the ocean, including scenarios with salty water containing 10 wt% $MgSO_4$, seawater, or pure water. Using these properties one can estimate the buoyancy power per unit mass available to drive convection in the subsurface oceans, following,

$$P_s = \frac{\alpha g q}{\rho C_p}. \tag{23}$$

Our estimates are given in Table 2. To generate synthetic residual and zonal spectra of the subsurface oceans, we follow the same approach as in our numerical experiments: the turbulent mixing is given by the buoyancy power $\Pi = P_s$, the β parameter is estimated at the mean equatorial radius following Eq. (19), with $r_o = R - D_I$ and $r_i = r_o - D$, the residual constant is $C_R = 5$ and the lower and upper bounds of the zonal constant are considered to be $0.3 \lesssim C_Z \lesssim 2.7$ (we recall that these bounds are derived from a vast collection of current as well as prior experiments and observations). At this stage, theoretical spectra can be produced using Eq. (10a)–(10b), but we still need to determine the range of wavenumbers over which the theory is applicable.

In zonostrophic turbulence, we can assume that the theoretical zonal spectrum is applicable between the Rhines scale k_{Rh} and the viscous dissipative scale denoted by k_ν. Conversely, the residual spectrum applies within the range from the Rhines scale (k_{Rh}) to the injection scale k_i^E. Outside of these scale ranges, the energy density systematically decreases. The viscous dissipative scale is known to be of millimetric order as in the Earth's ocean. This prompts us to assume that $k_\nu \gg k_{Rh}$. As such, we can estimate the energy of the residual and zonal velocities of the subsurface oceans by integrating the theoretical spectra in Eq. (10a)–(10b) between wavenumbers k_{Rh} and k_i,

$$E_R^s = \frac{3 C_R P_s^{2/3}}{2\pi^{2/3}} [L_{Rh}^{2/3} - L_i^{2/3}] \quad \text{and} \quad E_Z^s = \frac{C_Z \beta^2 L_{Rh}^4}{4\pi^4}, \tag{24}$$

where we have assumed that $k_{Rh} = \pi / L_{Rh}$. The typical magnitudes of the residual and zonal velocities, are obtained using the expressions $U_r = \sqrt{2E_R^s}$ and $U_z = \sqrt{2E_Z^s}$. The injection scale L_i which enters the residual velocity can be estimated using the critical azimuthal wavenumber at onset (Barik et al., 2023). Since $L_i \sim E^{1/3} D$ in the limit of $E \ll 1$ relevant to the icy satellites, L_i is expected to be 3 to 4 orders of magnitude smaller than the ocean thickness. Unfortunately, direct measurements of the Rhines scale, indicative of jet sizes, are unattainable due to the unobservable nature of the flow beneath the ice crusts of the satellites.

To tackle this challenge, an upper bound for the jets velocity can be derived from the energetics of the convective flow, i.e. an equilibrium between the injected buoyancy power per unit mass and dissipative processes (Jansen et al., 2023). Further assuming that dissipation can be mostly attributed to the drag of the zonal flows near the boundaries $\mathcal{F}_J(U_z)$ yields

$$\mathcal{F}_J(U_z) \sim P_s\,. \tag{25}$$

To account for the latter, Jansen (2016) assumed a parameterized turbulent quadratic drag of the form $\mathcal{F}_J(U_z) \approx C_D D U_z^3$. Using drag coefficients C_D calibrated to model the Earth's ocean, Jansen et al. (2023) and Kang (2024) then provide zonal flow velocity estimates ranging from a few mm/s for Enceladus to a few cm/s for Europa.

The applicability of such quadratic boundary drag formulation to the subsurface oceans of the icy satellites remains however unclear. In particular, outside the tangent cylinder, friction processes mostly involve the drag of quasi-geostrophic zonal jets on the external liquid–ice interface. Since the surface roughness of such ice caps is currently unknown, estimates for the drag coefficients remain speculative.

In light of these considerations, we here rather assume that dissipation mostly occurs via Ekman friction at the external boundary. This frictional mechanism can be conceptualized as the dissipation of energy by the Ekman layer with a typical thickness $\epsilon = \sqrt{\nu/\Omega}$ under no-slip boundary conditions. Based on the formulation of Ekman pumping by Greenspan (1968) and assuming flow geostrophy in a spherical shell, we derive in Appendix A the following formulation

$$\mathcal{F}_J(U_z) = \frac{(r_o \nu \Omega)^{1/2}}{\left(r_o^2 - s^2\right)^{3/4}} U_z^2, \tag{26}$$

which holds for $s \geq r_i$ (see, e.g. Gillet and Jones, 2006). This enables us to get an upper bound for the geostrophic zonal flow velocity which does not involve an arbitrary drag coefficient

$$\max(U_z) = \sqrt{P_s \frac{\left(r_o^2 - s_{\text{mid}}^2\right)^{3/4}}{r_o^{1/2}(\nu\Omega)^{1/2}}}. \tag{27}$$

The geometric factor $\left(r_o^2 - s_{\text{mid}}^2\right)^{3/4}$ is estimated at mid-radius, as is done for the β parameter in Eq. (19). It is essential to note that this formulation is only applicable outside the tangent cylinder, where zonal jets primarily develop in our numerical simulations. Also, the derivation of Eq. (27) does not account for possible large-scale topography that would make the upper boundary non-spherical. Assuming that the energy injected by buoyancy power is transferred upscale through non-linear processes and that Ekman friction serves as the physical mechanism arresting the upscale transfer of energy, Ekman friction defines the largest scale of the system, namely the Rhines scale L_{Rh}. In other words, we can solve for the Rhines scale in Eq. (24), considering $\max(U_z)$ from Eq. (27) as the upper bound for the zonal velocity.

Similar to velocity estimates, one should regard Rhines scale predictions as upper bounds. In addition, solving for Eqs. (24) and (27) does not prevent the Rhines scale from exceeding the ocean depth ($L_{Rh} > D$). Such predictions are inherently overestimated, since our derivation of the upper bound for the zonal velocity overlook Ekman friction inside the tangent cylinder (refer to Appendix A). The changes of $h(s)$ across the tangent cylinder prevent determining a unique relevant value for the zonal velocity upper bound that would incorporate stresses from both inside and outside the tangent cylinder. Hence, in the ongoing analysis, Rhines scale predictions must be regarded as possibly overestimated when exceeding the ocean depth. With this limitation in mind, we present in Table 2 our estimates for each satellite of the upper bound of the geostrophic zonal velocity $\max(U_z)$, the associated Rhines scale L_{Rh} and the residual velocity derived from Eq. (24).

Ganymede, with an ocean which could be as thick as 518 km, stands out as the most promising candidate for generating strong zonal jets. The upper bound for geostrophic zonal velocity reaches over 1 m/s, while the associated residual velocity remains at approximately 0.06 m/s. When the ocean depth is reduced to 119 km, the zonal velocity decreases to $\sim$ 0.3 m/s, and the residual velocity drops to around $\sim$ 0.016 m/s. In summary, Ganymede can possibly host strong zonal jets, with zonal velocities falling within the range of $0.3 \lesssim U_z \lesssim 1.66$ m/s, encompassing all fluid depth configurations. Europa and Titan follow with a zonal velocity range of $0.2 \lesssim U_z \lesssim 0.6$ m/s and $0.1 \lesssim U_z \lesssim 0.8$ m/s respectively, while Enceladus has a reduced zonal velocity falling within the range of $0.003 \lesssim U_z \lesssim 0.05$ m/s. We emphasize that these predictions for the zonal velocity only account for the geostrophic component of the flow.

Our predictions for zonal velocities are lower than those provided by Vance et al. (2021), which reach up to $U_z \sim 6$ m/s and $U_r \sim 0.11$ m/s for Ganymede. On the other hand, our estimates indicate larger velocities compared to the ranges reported by Bire et al. (2022), who suggest values between $10^{-3} \lesssim U_z \lesssim 0.7$ m/s and $10^{-2} \lesssim U_r \lesssim 0.5$ m/s. In both cases, estimations of flow velocities were solely based on the assumption that the Rossby numbers from numerical simulations, are equivalent to those in the oceans of icy satellites. This reasoning ignores a rescaling of the physical quantities using either scaling laws for the velocity (e.g. Gastine et al., 2016) or spectral analyses as done here. These numerical setups also present different geometries (a spherical shell for Vance et al. (2021) and a spherical wedge shell for Bire et al. (2022)) and mechanical boundary conditions that may explain the discrepancies. For comparison, Tyler (2008) demonstrated that tidal forcing on subsurface oceans triggers large-amplitude Rossby waves with typical velocities ranging from 0.086 to 0.84 m/s.

As already mentioned, Jansen et al. (2023) and Kang (2024) derived an upper bound for the zonal flow velocity using a power balance between the buoyancy power and boundary friction. Their parameterized turbulent boundary layer friction yields velocity estimates for Enceladus and Europa roughly 5 times lower than ours, a stark contrast to which we shall come back in the discussion below.

Our velocity predictions are associated with projections of the Rhines scale, whose uncertainty is contingent upon the zonal constant ($0.3 \lesssim C_Z \lesssim 2.7$). On Europa, the typical jets size falls within the range $0.7D \lesssim L_{Rh} \lesssim 1.4D$ on average. The lower estimate suggests ocean dynamics resembling our simulation at $E = 10^{-6}$ and $Ra = 2 \times 10^{10}$ presented in Fig. 5, where the prograde equatorial jet spans more than half of the ocean depth. The upper estimate, however, suggests a single equatorial jet whose typical size approaches the ocean depth. If such a configuration has been reported in numerical models with free-slip boundary conditions (Soderlund, 2019), it remains to be seen under no-slip conditions in the presence of Ekman friction. With Rhines scale predictions in the range $0.9D \lesssim L_{Rh} \lesssim 1.6D$ on average, Ganymede also appears to be a promising candidate for a single-jet solution outside the tangent cylinder. For Enceladus, however, the typical jets size is reduced to the range $0.15D \lesssim L_{Rh} \lesssim 0.3D$, indicating ocean dynamics reminiscent of our multiple jets simulation at $E = 10^{-6}$ and $Ra = 5 \times 10^9$, or possibly $Ra = 10^9$ (refer to Fig. 5). Discussing the size of jets on Titan is more intricate since our predictions consistently yield $L_{Rh} > D$. Our overall Rhines scale predictions is in line with the regime diagram presented in Fig. 1: smaller Rossby numbers and hence smaller jets in Enceladus reflect the stronger influence of rotation on its ocean dynamics. In contrast, Europa, Ganymede and Titan, straddling the transitional and non-rotational regimes, likely exhibit much larger zonal jets.

In our analysis, Eq. (24) also provides an estimate of the residual velocity. Across all satellites, the residual velocity is approximately one order of magnitude lower than the zonal velocity, reaching a magnitude of few mm/s. These estimates arise from integrating the residual spectrum over the range $k_{Rh} \leq k \leq k_i^E$. In the predictions of the residual velocity, the uncertainty stems from the determination of the Rhines scale, influenced by the uncertainty in C_Z, which yields standard deviations of the order $\approx 5 \times 10^{-3}$ m/s for Titan, Europa, and Ganymede, and $\approx 5 \times 10^{-4}$ m/s for Enceladus.

Fig. 12 provides a comprehensive summary of our numerical simulations and predictive findings. It shows the zonal Rossby number $Ro_Z = U_z/\Omega D$ together with the residual Rossby number $Ro_R = U_r/\Omega D$ computed from our numerical simulations and velocity predictions. The size of the coloured polygons reflect the uncertainties on internal properties and water compositions. These diagrams illustrate that in our numerical simulations, a decrease in the Ekman number strengthens the zonal Rossby number at the expense of the residual one. For $E = 10^{-6}$, flows obtained in numerical simulations correspond to $Ro_R \approx Ro_Z$. Our predictions indicate that this trend continues for the icy satellites, ultimately reaching a state where $Ro_Z \gg Ro_R$. In such a regime, the turbulence is strongly zonostrophic, and the Rhines scale is much larger than the transitional scale ($L_{Rh} \gg L_\beta$, see Table 2). In some cases,

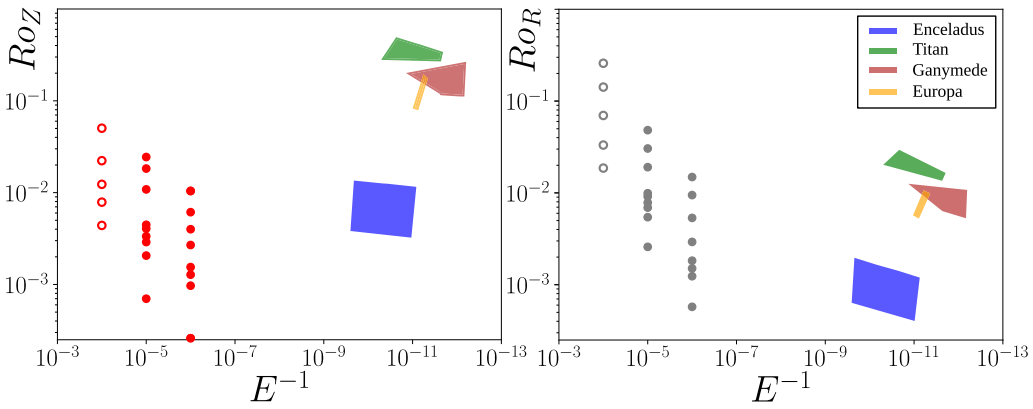

Fig. 12. Regime diagrams using Rossby and Ekman numbers from the simulations (dots) and predictions of the subsurface oceans (polygons). The left panel corresponds to the zonal velocity (Ro_Z), while the right one corresponds to the residual velocity (Ro_R). In each panel, the empty circles indicate values where $R_\beta < 1$, while the filled-in dots correspond to $R_\beta > 1$. (For interpretation of the references to colour in this figure legend, the reader is referred to the web version of this article.)

the theoretical zonostrophy index of the subsurface oceans (L_{Rh}/L_β) can even exceed ten (not reported here). However, it is important to note that this may not entirely reflect reality. As long as we only consider thermal convection, we overlook other sources of turbulence, such as mechanical and electromagnetic forcings, as well as double-diffusive convection (Tyler, 2008; Vance and Brown, 2005; Gissinger and Petitdemange, 2019). These supplementary sources will enhance the turbulent mixing within the subsurface oceans, likely reinforcing the residual energy of the flow, and consequently, modifying the zonal energy balance through cascade effects. Future numerical simulations could incorporate these additional energy sources, leading to a revision of the current version of our Rossby–Ekman diagram.

5. Discussion

We have investigated 21 numerical simulations of rapidly-rotating convection in a spherical shell of radius ratio $r_i/r_o = 0.8$, which is in the low range expected for the subsurface oceans in the Solar System. Extending previous numerical studies, we have explored a range of Ekman and Rayleigh numbers ($10^{-6} \leq E \leq 10^{-4}$ and $10^7 \leq Ra \leq 2{\times}10^{10}$) leading to the formation of multiple zonal jets with no-slip boundary conditions. At the lowest Ekman number, the kinetic energy contained in the zonal flow is comparable to the residual energy (see Fig. 3). This tendency would not have been so evident in earlier studies with Ekman numbers of $\mathcal{O}(10^{-4} - 10^{-5})$, if those studies did not assume free-slip boundary conditions.

We took advantage of our new numerical setup to extend the theory of zonostrophic turbulence to deep-seated convection in a rotating sphere. We recall that this theory has been developed in purely 2D-flows, thanks to numerical simulations on the sphere (Sukoriansky et al., 2002). Only recently has the theory of zonostrophic turbulence been extended to shallow-water simulations (Cabanes et al., 2020), mechanically forced laboratory experiments (Cabanes et al., 2017; Lemasquerier et al., 2023) and atmospheric observations (Young and Read, 2017). However, it is not obvious that this theory would also apply to deep-seated convection in a spherical shell where the β parameter substantially changes with the cylindrical radius.

To assess its applicability, we develop a flow decomposition in spectral space using cylindrical harmonic functions, namely the Hankel and Weber–Orr transforms. We argue that, given the axial symmetry of the zonal jets about the rotation axis, cylindrical harmonics are better suited for deep models of rapidly-rotating turbulence in spherical geometry. Thanks to this spectral analysis, we show that both zonal and residual flow components are well accounted for by the theory of zonostrophic turbulence for simulations with $E \leq 10^{-5}$ and within the limits of the Rayleigh numbers explored in this study. For $E \leq 10^{-5}$, present day numerical models cannot effectively reach the non-rotating limit depicted in Fig. 1, which precludes the exploration of the plausible failure of zonostrophic theory in this regime. We also stress that only the geostrophic component of the zonal energy was found to adhere to the zonostrophic theory. These different factors introduce uncertainties regarding the applicability of the zonostrophic theory when trending towards the non-rotating limit of the diagram, a region susceptible to be relevant for several subsurface oceans. Within these limits, our study demonstrates that it is possible to evaluate the residual and the geostrophic zonal energy of the flow by estimating the available buoyancy power of the convecting fluid, its Ekman number, and an estimate of the β parameter.

Assuming that the framework of zonostrophic turbulence can be extrapolated to the more extreme parameters of the icy satellites, we deliver in Table 2 velocity predictions for four subsurface oceans, namely, Enceladus, Titan, Europa, and Ganymede. Due to the lack of direct constraint on the jets size, necessary for estimating the zonal energy using zonostrophy theory, we define an upper bound for the zonal velocity using energetic constraints in the same vein as Jansen et al. (2023). This methodology allows us to predict the Rhines scale for each satellite, along with its residual energy.

We demonstrate that Europa and Ganymede may exhibit zonal jets with a typical size approaching the ocean depth, while Enceladus is likely characterized by multiple jets located outside the tangent cylinder. Predictions for Titan present additional challenges, as our jet size estimates consistently exceed the ocean depth. This poses a complication, given that our theoretical approach is built upon the assumption of zonal jets confined outside the tangent cylinder, and given that there is no evidence of numerical models with rigid boundaries developing jets broader than the shell thickness. Furthermore, our analysis reveals that for subsurface oceans, the upper bound for the geostrophic zonal velocities ranges from ~ 0.1 to 1.6 m/s, while the residual velocities do not exceed $\sim$ 0.003 to 0.06 m/s. The exception may be Enceladus, the smallest of the four satellites, whose zonal velocity ranges from ~ 0.003 to 0.05 m/s and residual velocity ranges from $\sim$ 0.0005 to 0.004 m/s. We emphasize that our estimates of the zonal velocity rests entirely on the geostrophic component of the flow. Ageostrophic contributions can further enhance our estimates, prompting the need for additional investigations in that regard.

Our theoretical approach places a primary focus on the kinetic energy budget within convective flows. It is similar to the approach of Jansen et al. (2023), while diverging from earlier analyses that simply assumed a direct equivalence between the Rossby number in numerical simulations and that in real oceanic flows (e.g. Amit et al.,

2020; Soderlund, 2019; Bire et al., 2022). The difference between our study and those by Jansen et al. (2023) and Kang (2024) stands in the treatment of the boundary drag: while they retain a quadratic turbulent drag hypothesis initially tailored to model Earth's ocean, we rather assume that boundary friction is governed by Ekman pumping outside the tangent cylinder of the subsurface oceans. At this stage of our knowledge of the ice–water interface in these hidden ocean worlds, it is however fair to say that no definite argument can be provided in favour of one hypothesis or the other. This leaves us with a possible factor of 3−5 between both velocity upper bounds, a prospect for future investigations.

Additionally, it is worth noting that prior numerical simulations employing free-slip boundary conditions overlook Ekman friction, a process we underscore as crucial for stabilizing the jets. Without considering this frictional effect, zonal jets tend to equilibrate with viscous dissipation in the fluid bulk (refer to Eq. (A.2) in the Appendix A) and typically reach system scale (e.g. Soderlund, 2019). If we extrapolate to the Ekman numbers relevant to icy satellites, where fluid viscosity is significantly lower, we encounter unrealistic scenarios where the residual energy would become negligible compared to the zonal energy. This speculation is influenced by the findings of Soderlund (2019), who already demonstrated at $E = 3 \times 10^{-4}$ a partition of $E_Z \sim 100 E_R$, this factor of 100 being already comparable to our predictions for the subsurface oceans. Therefore, we advocate for the necessity of employing no-slip boundary conditions in simulating subsurface ocean dynamics.

One of the main outcome of this study is to provide a Rossby–Ekman diagram that emphasizes flow velocities independently of the nature of the energetic sources that drive the flow. This contrasts with the Rayleigh–Ekman diagram introduced by Gastine et al. (2016). Currently, this Rossby–Ekman diagram allows us to locate our numerical simulations alongside with the predictions for subsurface oceans. We identify a continuous regime transition along the Ekman axis, shifting from a non-zonostrophic or quasi-3D turbulent regime at $E = 10^{-4}$ to a zonostrophic turbulent regime at $E = 10^{-5}$ and 10^{-6}. The transition threshold occurs when the zonostrophy index equals one, as illustrated in Fig. 12 with the empty and filled-in circles. However, no such transition is observed along the Rossby axis, as the zonostrophy index remains above unity for all simulations at $E = 10^{-5}$ and 10^{-6}. This is due to the high computational cost of 3D turbulent experiments, which prevents us from further exploring low Ekman and high Rossby numbers $Ro \sim \mathcal{O}(1)$, a regime possibly relevant for icy satellites such as Titan, Ganymede, and Europa. Within this limit, the global fraction of non-geostrophic energy increases, prompting questions about the continued validity of zonostrophic theory. Further investigations are required to elucidate these uncertainties.

Consequently, we advocate further exploration of the regime diagrams presented in Figs. 1 and 12 through deep-seated turbulent experiments. This effort should aim to delineate the dynamical boundaries of the zonostrophic regime of turbulence. For this purpose, laboratory experiments offer the potential for more turbulent flows, elevating the current Rossby number, while quasi-geostrophic simulations can reduce the computational cost to explore lower Ekman numbers (see Barrois et al., 2022; Lemasquerier et al., 2023).

In conclusion, it is crucial to stress that the estimate of an upper bound for the zonal flow velocity is instrumental to bring some predictive power to the theory of zonostrophic turbulence. This is required by the absence of direct observational data regarding the size of ocean jets, or equivalently, the Rhines scale. To address this limitation, there is a possibility that direct measurements of surface heat transfer or ice topography may carry indications of the underlying jet flows and, by extension, their latitudinal size and location. This approach has been previously investigated in studies conducted by Soderlund et al. (2014), Kvorka et al. (2018), Amit et al. (2020), Kvorka and Čadek (2022) and Terra-Nova et al. (2023). Such measurements are planned for Europa and Ganymede, as they are the main targets of ESA's JUICE mission and NASA's Europa Clipper mission. Should these future missions yield information about the typical size of Europa's and Ganymede's ocean jets, they would offer additional invaluable constraints to enhance the accuracy of our theoretical predictions regarding flow velocities.

CRediT authorship contribution statement

Simon Cabanes: Writing – review & editing, Writing – original draft, Visualization, Validation, Supervision, Software, Methodology, Investigation, Formal analysis, Data curation, Conceptualization. **Thomas Gastine:** Writing – review & editing, Writing – original draft, Validation, Project administration, Methodology, Investigation, Funding acquisition, Formal analysis, Conceptualization. **Alexandre Fournier:** Writing – review & editing, Writing – original draft, Resources, Project administration, Investigation, Funding acquisition, Formal analysis.

Declaration of competing interest

The authors declare that they have no known competing financial interests or personal relationships that could have appeared to influence the work reported in this paper.

Data availability

Data will be made available on request.

Acknowledgements

The authors thank Wanying Kang and an anonymous reviewer for their suggestions that helped improve the manuscript. The authors acknowledge the support of the French Agence Nationale de la Recherche (ANR), under grant ANR-19-CE31-0019 (project RevEarth). Numerical computations were performed on the S-CAPAD/DANTE platform at IPGP. This work has been funded by ESA, France in the framework of EO Science for Society, through contract 4000127193/19/NL/IA (SWARM + 4D Deep Earth: Core).

Appendix A. A bound for the axisymmetric azimuthal velocity in the rapidly-rotating regime

In the rapidly-rotating, or quasi-geostrophic, regime, the s and ϕ components of the quasi-geostrophic velocity $\mathbf{u}^g$ are invariant in the direction of global rotation z. An equation for the time-evolution of the axisymmetric azimuthal velocity is obtained by averaging the Navier–Stokes equation

$$\rho \frac{\partial \mathbf{u}}{\partial t} + \rho(\mathbf{u}\cdot\nabla)\mathbf{u} + 2\rho\Omega\mathbf{e}_z \times \mathbf{u} = -\nabla P + \rho\nu\nabla^2\mathbf{u} + \rho\alpha T\mathbf{g}. \tag{A.1}$$

over a so-called geostrophic cylinder $C(s)$, whose cylindrical radius s is comprised between r_i and r_o. In the z direction, $C(s)$ extends between $z = -h^+ + \epsilon$ and $z = h^+ - \epsilon$, where $h^+ = \sqrt{r_o^2 - s^2}$ and ϵ is the thickness of the viscous Ekman boundary layer that develops over the no-slip outer spherical boundary. Denoting the average over $C(s)$ by $\langle\cdot\rangle_{C(s)}$, we obtain

$$\left[\frac{\partial}{\partial t} + (\nu\Omega)^{1/2}\frac{r_o^{1/2}}{h^{+3/2}} - \nu\left(\frac{1}{s^2}\frac{\partial}{\partial s}s^3\frac{\partial}{\partial s}\frac{1}{s}\right)\right]\langle u_\phi^g\rangle_{C(s)} = -\frac{1}{s^2}\left\langle \partial_s\left(s^2 u_s^g u_\phi^g\right)\right\rangle_{C(s)}. \tag{A.2}$$

A secondary flow, driven by the so-called Ekman pumping, occurs within Ekman boundary layers and permeates the bulk of the fluid (Greenspan, 1968). Ekman pumping is responsible for the second term on the left-hand side of Eq. (A.2), via the calculation of $\langle u_s^g\rangle_{C(s)}$, see e.g. Schaeffer and Cardin (2005) and Gillet and Jones (2006) for more details. The term on the right hand-side of Eq. (A.2) is the nonlinear

Table B.3
Summary of the properties of the subsurface oceans of the Jovian and Saturnian satellites (see Vance et al., 2018; Soderlund, 2019, and references therein for further details).

	Enceladus	Titan	Europa	Ganymede
g (m/s^2)	0.1	1.4	1.3	1.4
Ω (s^{-1})	5.3×10^{-5}	4.6×10^{-6}	2.1×10^{-5}	1.0×10^{-5}
ν (m^2/s)	1.8×10^{-6}	1.8×10^{-6}	1.8×10^{-6}	1.8×10^{-6}
κ (m^2/s)	1.4×10^{-7}	1.8×10^{-7}	1.6×10^{-7}	1.8×10^{-7}
R (km)	252	2575	1561	2631
		Ice Ih thickness, D_I (km)		
$MgSO_4$ 10 wt%	50, 10	149, 86, 58	30, 5	157, 9, 26
Seawater	50, 10	–	30, 5	–
Water	51, 10	141, 74, 50	30, 5	134, 70, 5
		Ocean thickness, D (km)		
$MgSO_4$ 10 wt%	13, 63	91, 333, 403	103, 131	24, 287, 493
Seawater	12, 55	–	99, 126	–
Water	11, 53	130, 369, 420	97, 124	119, 361, 518
		Heat flux, q (mW/m^2)		
$MgSO_4$ 10 wt%	16, 83	14, 17, 19	24, 123	15, 18, 25
Seawater	16, 82	–	23, 121	–
Water	16, 81	14, 18, 20	24, 119	16, 20, 107
		Density, ρ (10^3 kg/m^3)		
$MgSO_4$ 10 wt%	1.11, 1.11	1.20, 1.23, 1.24	1.15, 1.14	1.19, 1.23, 1.24
Seawater	1.02, 1.02	–	1.07, 1.07	–
Water	1.00, 1.00	1.11, 1.14, 1.14	1.04, 1.04	1.11, 1.14, 1.14
		Heat capacity, C_p (10^3 J/kg/K)		
$MgSO_4$ 10 wt%	3.6, 3.7	2.1, 2.5, 2.8	3.3, 3.5	2.1, 2.4, 3.0
Seawater	4.0, 4.0	–	3.8, 3.8	–
Water	4.2, 4.2	3.0, 3.5, 3.6	3.9, 3.9	3.0, 3.5, 3.7
		Thermal expansivity, α (10^{-4} K^{-1})		
$MgSO_4$ 10 wt%	1.2, 1.3	0.4, 2.1, 2.7	2.1, 2.3	−0.1, 1.9, 3.2
Seawater	0.1, 0.1	–	2.5, 2.5	–
Water	−0.5, −0.5	2.3, 4.0, 4.2	1.9, 1.9	2.2, 4.0, 4.4
		β parameter, β (10^{-10} m^{-1} s^{-1})		
$MgSO_4$ 10 wt%	80.21, 15.65	1.0, 0.27, 0.22	4.01, 3.14	0.68, 0.39
Seawater	87.0, 18.11	–	4.17, 3.26	–
Water	–	0.7, 0.24, 0.21	4.26, 3.32	1.66, 0.53, 0.37
		Dimensionless numbers		
$Pr=\nu/\kappa$	13	10	11	10
$E=\frac{\nu}{\Omega D^2}$	$10^{-12}-10^{-10}$	$10^{-12}-10^{-11}$	$[5-9]\times10^{-12}$	$10^{-13}-10^{-11}$
$Ra=\frac{\alpha g D^3 \Delta T}{\nu\kappa}$	$10^{16}-10^{20}$	$10^{19}-10^{24}$	$10^{23}-10^{24}$	$10^{22}-10^{24}$
$\eta=\frac{R-D_I}{R-D_I}\frac{\nu\kappa}{D}$	0.74 – 0.94	0.83 – 0.96	0.91 – 0.94	0.8 – 0.95

Reynolds stress term, that will be denoted by $\mathcal{R}$ in the following. The balance for the axisymmetric zonal energy is obtained by multiplying Eq. (A.2) by $\langle u_\phi^g\rangle_{C(s)}$,

$$\frac{\partial}{\partial t}\left(\frac{1}{2}\langle u_\phi^g\rangle_{C(s)}^2\right) = \mathcal{R}\langle u_\phi^g\rangle_{C(s)} - (\nu\Omega)^{1/2}\frac{r_o^{1/2}}{h^{+3/2}}\langle u_\phi^g\rangle_{C(s)}^2 + \nu\left[\frac{1}{s^2}\frac{\partial}{\partial s}s^3\frac{\partial}{\partial s}\left(\frac{\langle u_\phi^g\rangle_{C(s)}}{s}\right)\right]\langle u_\phi^g\rangle_{C(s)}.$$

The axisymmetric zonal energy can increase in response to the first term on the right-hand side, and gets dissipated either by Ekman friction arising from the Coriolis term or by viscous stresses. We shall assume that the former is more effective at dissipating energy at the scale of jets than the latter. On time average, this implies that

$$\left|\overline{\mathcal{R}\langle u_\phi^g\rangle_{C(s)}}\right| \approx (\nu\Omega)^{1/2}\frac{r_o^{1/2}}{h^{+3/2}}\overline{\langle u_\phi^g\rangle_{C(s)}^2}. \tag{A.3}$$

Assuming that all energy injected by the mean buoyancy power $P_s = \alpha g q/\rho C_p$ is channelled into the zonal jets through nonlinear processes, namely that $\left|\mathcal{R}\langle u_\phi^g\rangle_{C(s)}\right| = P_s$, we derive an upper bound for the axisymmetric quasi-geostrophic zonal velocity,

$$\overline{\langle u_\phi^g\rangle_{C(s)}} \approx \sqrt{P_s\frac{\left(r_o^2-s^2\right)^{3/4}}{r_o^{1/2}(\nu\Omega)^{1/2}}}. \tag{A.4}$$

In the main text, this upper bound of the zonal velocity is denoted by $\max(U_z)$. The geometric factor $\left(r_o^2-s^2\right)^{3/4}$ is estimated at mid-radius, as is done for the β parameter in Eq. (19).

Appendix B. Properties of the subsurface oceans

All the relevant properties of the icy satellites are reported in Table B.3. Building upon the methodology outlined by Soderlund (2019) we can anticipate the convective regime of the icy satellites by estimating their Ekman, Rayleigh, and Prandtl numbers. The Prandtl number, which solely depends on the properties of the fluid, is approximated to be around $Pr \sim 10$ for the oceans of the satellite (Abramson et al., 2001; Nayar et al., 2016). Calculating the Ekman number is also relatively straightforward, as it only depends on fluid viscosity, the rotation rate, and ocean depth (here the interior model from Vance et al., 2018, is employed). Following on from Soderlund (2019), the Rayleigh number requires the knowledge of the superadiabatic temperature contrast ΔT. Soderlund (2019) suggests to solve for ΔT algebraically considering both non-rotating and rapidly-rotating scaling laws for the heat flux q. The temperature contrast considering a non-rotating regime is,

$$\Delta T = 7.3\left(\frac{\nu}{\alpha g\rho C_p}\right)^{1/4} q^{3/4}, \tag{B.1}$$

and for the rotating regime,

$$\Delta T = 2.1 \left(\frac{\Omega^4 \kappa}{\rho^2 C_p^2 \nu \alpha^3 g^3} \right)^{1/5} (q^2 D)^{1/5}, \quad \text{(B.2)}$$

see also Gastine et al. (2016) for more details. Note that the range of values for the dimensionless quantities given in Table B.3 correspond to the estimated minima and maxima.

References

Abramson, E.H., Brown, J.M., Slutsky, L.J., 2001. The thermal diffusivity of water at high pressures and temperatures. J. Chem. Phys. 115 (22), 10461–10463. http://dx.doi.org/10.1063/1.1418244.

Amit, H., Choblet, G., Tobie, G., Terra-Nova, F., Čadek, O., Bouffard, M., 2020. Cooling patterns in rotating thin spherical shells - application to titan's subsurface ocean. Icarus 338, 113509. http://dx.doi.org/10.1016/j.icarus.2019.113509.

Ascher, U.M., Ruuth, S.J., Spiteri, R.J., 1997. Implicit-explicit runge-kutta methods for time-dependent partial differential equations. Appl. Numer. Math. 25, 151–167. http://dx.doi.org/10.1016/S0168-9274(97)00056-1.

Aurnou, J.M., Olson, P.L., 2001. Strong zonal winds from thermal convection in a rotating spherical shell. Geophys. Res. Lett. 28 (13), 2557–2559. http://dx.doi.org/10.1029/2000GL012474.

Baddour, N., 2019. The discrete Hankel transform. In: Nikolic, G.S., Marković-Nikolić, D.Z. (Eds.), Fourier Transforms-Century of Digitalization and Increasing Expectations. IntechOpen, Rijeka, pp. 1–23. http://dx.doi.org/10.5772/intechopen.84399.

Barik, A., Triana, S.A., Calkins, M., Stanley, S., Aurnou, J., 2023. Onset of convection in rotating spherical shells: Variations with radius ratio. Earth Space Sci. 10 (1), http://dx.doi.org/10.1029/2022EA002606, e2022EA002606.

Barrois, O., Gastine, T., Finlay, C.C., 2022. Comparison of quasi-geostrophic, hybrid and 3-D models of planetary core convection. Geophys. J. Int. 231 (1), 129–158. http://dx.doi.org/10.1093/gji/ggac141.

Bekki, Y., Cameron, R.H., Gizon, L., 2022. Theory of solar oscillations in the inertial frequency range: Amplitudes of equatorial modes from a nonlinear rotating convection simulation. Astron. Astrophys. 666, A135. http://dx.doi.org/10.1051/0004-6361/202244150.

Bire, S., Kang, W., Ramadhan, A., Campin, J.-M., Marshall, J., 2022. Exploring ocean circulation on icy moons heated from below. J. Geophys. Res. (Planets) 127 (3), e07025. http://dx.doi.org/10.1029/2021JE007025.

Boer, G.J., 1983. Homogeneous and isotropic turbulence on the sphere. J. Atmos. Sci. 40 (1), 154–163. http://dx.doi.org/10.1175/1520-0469(1983)040<0154:HAITOT>2.0.CO;2.

Boffetta, G., Ecke, R.E., 2012. Two-dimensional turbulence. Annu. Rev. Fluid Mech. 44, 427–451. http://dx.doi.org/10.1146/annurev-fluid-120710-101240.

Böning, V.G.A., Wulff, P., Dietrich, W., Wicht, J., Christensen, U.R., 2023. Direct driving of simulated planetary jets by upscale energy transfer. Astron. Astrophys. 670, A15. http://dx.doi.org/10.1051/0004-6361/202244278.

Boyd, J.P., Yu, F., 2011. Comparing seven spectral methods for interpolation and for solving the Poisson equation in a disk: Zernike polynomials, Logan-Shepp ridge polynomials, Chebyshev-Fourier series, cylindrical robert functions, Bessel-Fourier expansions, square-to-disk conformal mapping and radial basis functions. J. Comput. Phys. 230 (4), 1408–1438. http://dx.doi.org/10.1016/j.jcp.2010.11.011.

Cabanes, S., Aurnou, J., Favier, B., Le Bars, M., 2017. A laboratory model for deep-seated jets on the gas giants. Nat. Phys. 13 (4), 387–390. http://dx.doi.org/10.1038/nphys4001.

Cabanes, S., Spiga, A., Young, R.M., 2020. Global climate modeling of Saturn's atmosphere. Part III: Global statistical picture of zonostrophic turbulence in high-resolution 3D-turbulent simulations. Icarus 345, 113705. http://dx.doi.org/10.1016/j.icarus.2020.113705.

Carlson, R.W., Calvin, W.M., Dalton, J.B., Hansen, G.B., Hudson, R.L., Johnson, R.E., McCord, T.B., Moore, M.H., 2009. Europa's surface composition. In: Pappalardo, R.T., B., M.W., Khurana, K.K. (Eds.), Europa. University of Arizona Press, Tucson, pp. 283–328. http://dx.doi.org/10.2307/j.ctt1xp3wdw.18.

Cheng, J.S., Aurnou, J.M., Julien, K., Kunnen, R.P.J., 2018. A heuristic framework for next-generation models of geostrophic convective turbulence. Geophys. Astrophys. Fluid Dyn. 112 (4), 277–300. http://dx.doi.org/10.1080/03091929.2018.1506024.

Christensen, U.R., 2002. Zonal flow driven by strongly supercritical convection in rotating spherical shells. J. Fluid Mech. 470 (1), 115–133. http://dx.doi.org/10.1017/S0022112002002008.

Christensen, U.R., Aubert, J., 2006. Scaling properties of convection-driven dynamos in rotating spherical shells and application to planetary magnetic fields. Geophys. J. Int. 166 (1), 97–114. http://dx.doi.org/10.1111/j.1365-246X.2006.03009.x.

Cinelli, G., 1965. An extension of the finite Hankel transform and applications. Internat. J. Engrg. Sci. 3 (5), 539–559. http://dx.doi.org/10.1016/0020-7225(65)90034-0.

Deusebio, E., Boffetta, G., Lindborg, E., Musacchio, S., 2014. Dimensional transition in rotating turbulence. Phys. Rev. E 90 (2), 023005. http://dx.doi.org/10.1103/PhysRevE.90.023005.

Dormy, E., Soward, A., Jones, C., Jault, D., Cardin, P., 2004. The onset of thermal convection in rotating spherical shells. J. Fluid Mech. 501, 43–70. http://dx.doi.org/10.1017/s0022112003007316.

Favier, B., Silvers, L.J., Proctor, M.R., 2014. Inverse cascade and symmetry breaking in rapidly rotating Boussinesq convection. Phys. Fluids 26 (9), http://dx.doi.org/10.1063/1.4895131.

Galperin, B., Hoemann, J., Espa, S., Di Nitto, G., Lacorata, G., 2016. Anisotropic macroturbulence and diffusion associated with a westward zonal jet: From laboratory to planetary atmospheres and oceans. Phys. Rev. E 94 (6), 063102. http://dx.doi.org/10.1103/PhysRevE.94.063102.

Galperin, B., Sukoriansky, S., Dikovskaya, N., 2010. Geophysical flows with anisotropic turbulence and dispersive waves: flows with a β-effect. Ocean Dyn. 60 (2), 427–441. http://dx.doi.org/10.1007/s10236-010-0278-2.

Galperin, B., Sukoriansky, S., Dikovskaya, N., Read, P., Yamazaki, Y., Wordsworth, R., 2006. Anisotropic turbulence and zonal jets in rotating flows with a β-effect. Nonlinear Process. Geophys. 13 (1), 83–98. http://dx.doi.org/10.5194/npg-13-83-2006.

Galperin, B., Young, R.M., Sukoriansky, S., Dikovskaya, N., Read, P.L., Lancaster, A.J., Armstrong, D., 2014. Cassini observations reveal a regime of zonostrophic macroturbulence on Jupiter. Icarus 229, 295–320. http://dx.doi.org/10.1016/j.icarus.2013.08.030.

Gastine, T., Aurnou, J.M., 2023. Latitudinal regionalization of rotating spherical shell convection. J. Fluid Mech. 954, R1. http://dx.doi.org/10.1017/jfm.2022.1010, arXiv:2211.17055.

Gastine, T., Heimpel, M., Wicht, J., 2014. Zonal flow scaling in rapidly-rotating compressible convection. Phys. Earth Planet. Inter. 232, 36–50. http://dx.doi.org/10.1016/j.pepi.2014.03.011.

Gastine, T., Wicht, J., Aubert, J., 2016. Scaling regimes in spherical shell rotating convection. J. Fluid Mech. 808, 690–732. http://dx.doi.org/10.1017/jfm.2016.659.

Gillet, N., Jones, C.A., 2006. The quasi-geostrophic model for rapidly rotating spherical convection outside the tangent cylinder. J. Fluid Mech. 554, 343–369. http://dx.doi.org/10.1017/S0022112006009219.

Gilman, P.A., 1977. Nonlinear dynamics of Boussinesq convection in a deep rotating spherical shell-I. Geophys. Astrophys. Fluid Dyn. 8 (1), 93–135. http://dx.doi.org/10.1080/03091927708240373.

Gissinger, C., Petitdemange, L., 2019. A magnetically driven equatorial jet in Europa's ocean. Nat. Astron. 3 (5), 401–407. http://dx.doi.org/10.1038/s41550-019-0713-3.

Gizon, L., Cameron, R.H., Bekki, Y., Birch, A.C., Bogart, R.S., Brun, A.S., Damiani, C., Fournier, D., Hyest, L., Jain, K., et al., 2021. Solar inertial modes: Observations, identification, and diagnostic promise. Astron. Astrophys. 652, L6. http://dx.doi.org/10.1051/0004-6361/202141462.

Gopinath, V., Fournier, A., Gastine, T., 2022. An assessment of implicit-explicit time integrators for the pseudo-spectral approximation of Boussinesq thermal convection in an annulus. J. Comput. Phys. 460, 110965. http://dx.doi.org/10.1016/j.jcp.2022.110965.

Grannan, A.M., Favier, B., Le Bars, M., Aurnou, J.M., 2017. Tidally forced turbulence in planetary interiors. Geophys. J. Int. 208 (3), 1690–1703. http://dx.doi.org/10.1093/gji/ggw479.

Grasset, O., Dougherty, M., Coustenis, A., Bunce, E., Erd, C., Titov, D., Blanc, M., Coates, A., Drossart, P., Fletcher, L., et al., 2013. Jupiter ICy moons explorer (JUICE): An ESA mission to orbit ganymede and to characterise the Jupiter system. Planet. Space Sci. 78, 1–21. http://dx.doi.org/10.1016/j.pss.2012.12.002.

Greenspan, H.P., 1968. The Theory of Rotating Fluids, vol. 327, Cambridge University Press Cambridge.

Guervilly, C., Cardin, P., 2017. Multiple zonal jets and convective heat transport barriers in a quasi-geostrophic model of planetary cores. Geophys. J. Int. 211 (1), 455–471. http://dx.doi.org/10.1093/gji/ggx315.

Guizar-Sicairos, M., Gutiérrez-Vega, J.C., 2004. Computation of quasi-discrete Hankel transforms of integer order for propagating optical wave fields. J. Opt. Soc. Amer. A 21 (1), 53–58. http://dx.doi.org/10.1364/JOSAA.21.000053.

Heimpel, M., Aurnou, J., 2007. Turbulent convection in rapidly rotating spherical shells: A model for equatorial and high latitude jets on Jupiter and Saturn. Icarus 187 (2), 540–557. http://dx.doi.org/10.1016/j.icarus.2006.10.023.

Heimpel, M., Aurnou, J., Wicht, J., 2005. Simulation of equatorial and high-latitude jets on Jupiter in a deep convection model. Nature 438 (7065), 193–196. http://dx.doi.org/10.1038/nature04208.

Hsu, H.W., Postberg, F., Sekine, Y., Shibuya, T., Kempf, S., Horányi, M., Juhász, A., Altobelli, N., Suzuki, K., Masaki, Y., et al., 2015. Ongoing hydrothermal activities within enceladus. Nature 519 (7542), 207–210. http://dx.doi.org/10.1038/nature14262.

Huang, H.P., Galperin, B., Sukoriansky, S., 2001. Anisotropic spectra in two-dimensional turbulence on the surface of a rotating sphere. Phys. Fluids 13 (1), 225–240. http://dx.doi.org/10.1063/1.1327594.

Jansen, M.F., 2016. The turbulent circulation of a snowball earth ocean. J. Phys. Oceanogr. 46 (6), 1917–1933. http://dx.doi.org/10.1175/JPO-D-15-0224.1.

Jansen, M.F., Kang, W., Kite, E.S., Zeng, Y., 2023. Energetic constraints on ocean circulations of icy ocean worlds. Planet. Sci. J. 4 (6), 117. http://dx.doi.org/10.3847/PSJ/acda95.

Kang, W., 2024. Nonsynchronous rotation of icy moon ice shells: The thermal wind perspective. Sci. Adv. 10 (4), eadk2277. http://dx.doi.org/10.1126/sciadv.adk2277.

Kang, W., Mittal, T., Bire, S., Campin, J.M., Marshall, J., 2022. How does salinity shape ocean circulation and ice geometry on enceladus and other icy satellites? Sci. Adv. 8 (29), eabm4665. http://dx.doi.org/10.1126/sciadv.abm4665.

Kraichnan, R.H., 1967. Inertial ranges in two dimensional turbulence. Phys. Fluids 10 (7), 1417–1423. http://dx.doi.org/10.1063/1.1762301.

Kunnen, R.P., Ostilla-Mónico, R., Van Der Poel, E.P., Verzicco, R., Lohse, D., 2016. Transition to geostrophic convection: the role of the boundary conditions. J. Fluid Mech. 799, 413–432. http://dx.doi.org/10.1017/jfm.2016.394.

Kvorka, J., Čadek, O., 2022. A numerical model of convective heat transfer in titan's subsurface ocean. Icarus 376, 114853. http://dx.doi.org/10.1016/j.icarus.2021.114853.

Kvorka, J., Čadek, O., Tobie, G., Choblet, G., 2018. Does titan's long-wavelength topography contain information about subsurface ocean dynamics? Icarus 310, 149–164. http://dx.doi.org/10.1016/j.icarus.2017.12.010.

Lemasquerier, D., Favier, B., Le Bars, M., 2023. Zonal jets experiments in the gas giants' zonostrophic regime. Icarus 390, 115292. http://dx.doi.org/10.1016/j.icarus.2022.115292.

Lemasquerier, D., Grannan, A.M., Vidal, J., Cébron, D., Favier, B., Le Bars, M., Aurnou, J.M., 2017. Libration-driven flows in ellipsoidal shells. J. Geophys. Res.: Planets 122 (9), 1926–1950. http://dx.doi.org/10.1002/2017JE005340.

MacRobert, T.M., 1932. XVI.—Fourier integrals. Proc. Roy. Soc. Edinburgh 51, 116–126. http://dx.doi.org/10.1017/S0370164600023063.

Maffei, S., Krouss, M.J., Julien, K., Calkins, M.A., 2021. On the inverse cascade and flow speed scaling behaviour in rapidly rotating Rayleigh–Bénard convection. J. Fluid Mech. 913, A18. http://dx.doi.org/10.1017/jfm.2020.1058.

Nayar, K.G., Sharqawy, M.H., Banchik, L.D., et al., 2016. Thermophysical properties of seawater: A review and new correlations that include pressure dependence. Desalination 390, 1–24. http://dx.doi.org/10.1016/j.desal.2016.02.024.

Postberg, F., Khawaja, N., Abel, B., Choblet, G., Glein, C.R., Gudipati, M.S., Henderson, B.L., Hsu, H.W., Kempf, S., Klenner, F., et al., 2018. Macromolecular organic compounds from the depths of enceladus. Nature 558 (7711), 564–568. http://dx.doi.org/10.1038/s41586-018-0246-4.

Postberg, F., Schmidt, J., Hillier, J., Kempf, S., Srama, R., 2011. A salt-water reservoir as the source of a compositionally stratified plume on enceladus. Nature 474 (7353), 620–622. http://dx.doi.org/10.1038/nature10175.

Read, P.L., Jacoby, T.N.L., Rogberg, P.H.T., Wordsworth, R.D., Yamazaki, Y.H., Miki-Yamazaki, K., Young, R.M.B., Sommeria, J., Didelle, H., Viboud, S., 2015. An experimental study of multiple zonal jet formation in rotating, thermally driven convective flows on a topographic beta-plane. Phys. Fluids 27 (8), 085111. http://dx.doi.org/10.1063/1.4928697.

Rhines, P.B., 1975. Waves and turbulence on a beta-plane. J. Fluid Mech. 69 (3), 417–443. http://dx.doi.org/10.1017/s0022112075001504.

Roberts, J.H., McKinnon, W.B., Elder, C.M., Tobie, G., Biersteker, J.B., Young, D., Park, R.S., Steinbrügge, G., Nimmo, F., Howell, S.M., Castillo-Rogez, J.C., Cable, M.L., Abrahams, J.N., Bland, M.T., Chivers, C., Cochrane, C.J., Dombard, A.J., Ernst, C., Genova, A., Gerekos, C., Glein, C., Harris, C.D., Hay, H.C.F.C., Hayne, P.O., Hedman, M., Hussmann, H., Jia, X., Khurana, K., Kiefer, W.S., Kirk, R., Kivelson, M., Lawrence, J., Leonard, E.J., Lunine, J.I., Mazarico, E., McCord, T.B., McEwen, A., Paty, C., Quick, L.C., Raymond, C.A., Retherford, K.D., Roth, L., Rymer, A., Saur, J., Scanlan, K., Schroeder, D.M., Senske, D.A., Shao, W., Soderlund, K., Spiers, E., Styczinski, M.J., Tortora, P., Vance, S.D., Villarreal, M.N., Weiss, B.P., Westlake, J.H., Withers, P., Wolfenbarger, N., Buratti, B., Korth, H., Pappalardo, R.T., The Interior Thematic Working Group, 2023. Exploring the interior of europa with the europa clipper. Space Sci. Rev. 219 (6), 46. http://dx.doi.org/10.1007/s11214-023-00990-y.

Schaeffer, N., 2013. Efficient spherical harmonic transforms aimed at pseudospectral numerical simulations. Geochem. Geophys. Geosyst. 14 (3), 751–758. http://dx.doi.org/10.1002/ggge.20071.

Schaeffer, N., Cardin, P., 2005. Quasigeostrophic model of the instabilities of the Stewartson layer in flat and depth-varying containers. Phys. Fluids 17 (10), 104111. http://dx.doi.org/10.1063/1.2073547.

Schwaiger, T., Gastine, T., Aubert, J., 2021. Relating force balances and flow length scales in geodynamo simulations. Geophys. J. Int. 224 (3), 1890–1904. http://dx.doi.org/10.1093/gji/ggaa545.

Sneddon, I.N., 1946. III. Finite Hankel transforms. London, Edinb., Dublin Philos. Mag. J. Sci. 37 (264), 17–25. http://dx.doi.org/10.1080/14786444608521150.

Soderlund, K.M., 2019. Ocean dynamics of outer solar system satellites. Geophys. Res. Lett. 46 (15), 8700–8710. http://dx.doi.org/10.1029/2018gl081880.

Soderlund, K.M., Kalousová, K., Buffo, J.J., Glein, C.R., Goodman, J.C., Mitri, G., Patterson, G.W., Postberg, F., Rovira-Navarro, M., Rückriemen, T., et al., 2020. Ice-ocean exchange processes in the jovian and Saturnian satellites. Space Sci. Rev. 216, 1–57. http://dx.doi.org/10.1007/s11214-020-00706-6.

Soderlund, K.M., Schmidt, B.E., Wicht, J., Blankenship, D.D., 2014. Ocean-driven heating of Europa's icy shell at low latitudes. Nat. Geosci. 7 (1), 16–19. http://dx.doi.org/10.1038/ngeo2021.

Sukoriansky, S., Dikovskaya, N., Galperin, B., 2007. On the arrest of inverse energy cascade and the Rhines scale. J. Atmos. Sci. 64 (9), 3312–3327. http://dx.doi.org/10.1175/jas4013.1.

Sukoriansky, S., Galperin, B., Dikovskaya, N., 2002. Universal spectrum of two-dimensional turbulence on a rotating sphere and some basic features of atmospheric circulation on giant planets. Phys. Rev. Lett. 89 (12), 124501. http://dx.doi.org/10.1103/physrevlett.89.124501.

Terra-Nova, F., Amit, H., Choblet, G., Tobie, G., Bouffard, M., Čadek, O., 2023. The influence of heterogeneous seafloor heat flux on the cooling patterns of Ganymede's and Titan's subsurface oceans. Icarus 389, 115232. http://dx.doi.org/10.1016/j.icarus.2022.115232.

Tosi, F., ro Mura, A., Cofano, A., Zambon, F., Glein, C.R., Ciarniello, M., Lunine, J.I., Piccioni, G., Plainaki, C., Sordini, R., Adriani, A., Bolton, S.J., Hansen, C.J., Nordheim, T.A., Moirano, A., Agostini, L., Altieri, F., Brooks, S.M., Cicchetti, A., Dinelli, B.M., Grassi, D., Migliorini, A., Moriconi, M.L., Noschese, R., Scarica, P., Sindoni, G., Stefani, S., Turrini, D., 2023. Salts and organics on ganymede's surface observed by the JIRAM spectrometer onboard juno. Nat. Astron. http://dx.doi.org/10.1038/s41550-023-02107-5.

Tyler, R.H., 2008. Strong ocean tidal flow and heating on moons of the outer planets. Nature 456 (7223), 770–772. http://dx.doi.org/10.1038/nature07571.

Vance, S., Brown, J.M., 2005. Layering and double-diffusion style convection in europa's ocean. Icarus 177 (2), 506–514. http://dx.doi.org/10.1016/j.icarus.2005.06.005.

Vance, S.D., Panning, M.P., Stähler, S., Cammarano, F., Bills, B.G., Tobie, G., Kamata, S., Kedar, S., Sotin, C., Pike, W.T., et al., 2018. Geophysical investigations of habitability in ice-covered ocean worlds. J. Geophys. Res.: Planets 123 (1), 180–205. http://dx.doi.org/10.1002/2017je005341.

Vance, S.D., Styczinski, M., Bills, B., Cochrane, C., Soderlund, K., Gómez-Pérez, N., Paty, C., 2021. Magnetic induction responses of Jupiter's ocean moons including effects from adiabatic convection. J. Geophys. Res.: Planets 126 (2), http://dx.doi.org/10.1029/2020je006418, e2020JE006418.

Wang, Q., Ronneberger, O., Burkhardt, H., 2009. Rotational invariance based on Fourier analysis in polar and spherical coordinates. IEEE Trans. Pattern Anal. Mach. Intell. 31 (9), 1715–1722. http://dx.doi.org/10.1109/tpami.2009.29.

Wicht, J., 2002. Inner-core conductivity in numerical dynamo simulations. Phys. Earth Planet. Inter. 132 (4), 281–302. http://dx.doi.org/10.1016/s0031-9201(02)00078-x.

Wordsworth, R.D., Read, P.L., Yamazaki, Y.H., 2008. Turbulence, waves, and jets in a differentially heated rotating annulus experiment. Phys. Fluids 20 (12), 126602. http://dx.doi.org/10.1063/1.2990042.

Yadav, R.K., Bloxham, J., 2020. Deep rotating convection generates the polar hexagon on Saturn. Proc. Natl. Acad. Sci. 117 (25), 13991–13996. http://dx.doi.org/10.1073/pnas.2000317117.

Yadav, R.K., Gastine, T., Christensen, U.R., Duarte, L.D.V., Reiners, A., 2016. Effect of shear and magnetic field on the heat-transfer efficiency of convection in rotating spherical shells. Geophys. J. Int. 204 (2), 1120–1133. http://dx.doi.org/10.1093/gji/ggv506.

Young, R.M., Read, P.L., 2017. Forward and inverse kinetic energy cascades in Jupiter's turbulent weather layer. Nat. Phys. 13 (11), 1135. http://dx.doi.org/10.1038/nphys4227.